Multimode Characterization Approach for Understanding Cell-Level PV Performance and Degradation

Glenn Teeter

National Renewable Energy Laboratory

NREL is a national laboratory of the U.S. Department of Energy
Office of Energy Efficiency & Renewable Energy
Operated by the Alliance for Sustainable Energy, LLC

This report is available at no cost from the National Renewable Energy Laboratory (NREL) at www.nrel.gov/publications.

Contract No. DE-AC36-08GO28308

Technical Report
NREL/TP-5K00-84194
October 2022

Multimode Characterization Approach for Understanding Cell-Level PV Performance and Degradation

Glenn Teeter

National Renewable Energy Laboratory

Suggested Citation
Teeter, Glenn. 2022. *Multimode Characterization Approach for Understanding Cell-Level PV Performance and Degradation*. Golden, CO: National Renewable Energy Laboratory. NREL/TP-5K00-84194. https://www.nrel.gov/docs/fy23osti/84194.pdf

NREL is a national laboratory of the U.S. Department of Energy
Office of Energy Efficiency & Renewable Energy
Operated by the Alliance for Sustainable Energy, LLC

This report is available at no cost from the National Renewable Energy Laboratory (NREL) at www.nrel.gov/publications.

Contract No. DE-AC36-08GO28308

Technical Report
NREL/TP-5K00-84194
October 2022

National Renewable Energy Laboratory
15013 Denver West Parkway
Golden, CO 80401
303-275-3000 • www.nrel.gov

NOTICE

This work was authored by the National Renewable Energy Laboratory, operated by Alliance for Sustainable Energy, LLC, for the U.S. Department of Energy (DOE) under Contract No. DE-AC36-08GO28308. Funding provided by the U.S. Department of Energy Office of Energy Efficiency and Renewable Energy Solar Energy Technologies Office. The views expressed herein do not necessarily represent the views of the DOE or the U.S. Government.

Final Technical Report (FTR)

Agency/Office/Program	DOE/EERE/Solar Energy Technology Office	
Award Number	DE-EE34361	
Project Title	Multimode Characterization Approach for Understanding Cell-Level PV Performance and Degradation	
Principal Investigator	Glenn Teeter, Group Manager, glenn.teeter@nrel.gov, 303-384-6664	
Business Contact	Daniel Friedman, Photovoltaics Subprogram Manager, daniel.friedman@nrel.gov, 303-384-6472	
Submission Date	9/30/2022	
DUNS Number	805948051 + 0000	
Recipient Organization	National Renewable Energy Laboratory	
Project Period	**Start:** Oct. 1, 2018	**End:** June 30, 2022
Project Budget	Total $3630000 (DOE: $3630000; C/S: $0)	
Submitting Official Signature		

1 Acknowledgement

This material is based upon work supported by the U.S. Department of Energy's Office of Energy Efficiency and Renewable Energy (EERE) under the SETO National Laboratory Call DE-LC-000L044 Multiyear Project Proposal Award Number 34361.

2 Disclaimer

3 Executive Summary

Cell-level degradation processes impact the economic viability and large-scale deployment prospects for both established and emerging photovoltaic (PV) technologies. This project addresses the need to develop experimental and device-modeling approaches for studying cell-level degradation processes in photovoltaic (PV) devices using a variety of characterization techniques that provide access to complementary material and device properties. Our results demonstrate that by coupling characterization results with device modeling it is possible to develop comprehensive understanding of processes leading to performance limitations and degradation.

This project developed a suite of novel measurement techniques including pulsed-light-bias operando X-ray and photoelectron spectroscopy (popXPS), light-biased scanning microwave impedance microscopy (sMIM), and near-field transport imaging (TI). In addition, *operando* characterization methodologies and *in situ* stressing capabilities have been developed and applied for techniques including electron-beam-induced current (EBIC), cathodoluminescence (CL), and Kelvin probe force microscopy (KPFM). Device-physics models were developed and applied to simulate correlative, multi-mode measurements to extract material and device parameters that control performance degradation. These characterization and modeling techniques were applied in a multi-mode approach to probe cell-level degradation mechanisms in Cd(Se,Te) and hybrid perovskite PV devices. Together these efforts contribute to foundational PV degradation science by establishing a framework for understanding PV performance degradation at the cell level and benefit the U.S. PV industry by providing resources in the form of novel experimental capabilities, knowledge gained, and available expertise that can accelerate research and development of improved PV device materials and architectures.

The project provided a comprehensive understanding of degradation in baseline Cd(Se,Te) solar cells provided by our collaborators at Colorado State University (CSU). EBIC and CL-based measurements and revealed unusual collection and recombination profiles in these devices, which underwent significant changes during stressing. KPFM and operando XPS measurements showed that device stressing permanently alters energy-band alignments at the (Mg,Zn)O/Cd(Se,Te) interface, which in turn accounts for an observed loss in fill factor.

Studies on hybrid perovskite devices were hampered to a significant extent by delays related to the pandemic. Nevertheless, a set of hybrid perovskite devices (supplied through an NREL-industry partnership) were stress tested and characterized with techniques including EBIC, sMIM, popXPS/popUPS and optically excited TI. Available results from these measurements informed the device modeling effort and suggest that defects and related band offsets at the C60/LiF/hybrid perovskite interface are the primary source of degradation in these devices.

4 Table of Contents

5 Background

5.1 CdTe Stability and Degradation

Cu has long been used as a p-type dopant in CdTe PV devices as a means of improving device performance by helping to form a Ohmic back contact. Several recent studies of CdTe module-level degradation have focused on the detrimental effects of electromigration of various species, including Cu, under field operating conditions. For example, a recent study by Kettle et al. identified two main mechanisms related to Cu-containing back contacts.[1] The first is the commonly understood degradation mechanism of Cu migration from the back contact to the junction, where accumulation of Cu in the CdS layer is associated with losses in short-wavelength external quantum efficiency (EQE). The second mechanism is oxidation of the Te-rich layer at the back contact, which lowers efficiency by increasing series resistance. Hsu et al. examined the optimization of Cu doping in Cd(Se,Te)/CdTe solar cells.[2] The study found that excessive Cu incorporation, whether due to the amount of added Cu or to excessive annealing to promote Cu migration and activation, led to losses in initial performance that correlated with a reduction in minority-carrier lifetime. They also concluded that in general Cd(Se,Te)-based devices were more tolerant to excessive Cu content than were standard (Se-free) CdTe-based devices.

Other researchers have focused on degradation or performance optimization issues related to the junction or front current collector in CdTe devices. A recent study by Samoilenko et al. used combinatorial approaches to optimize processing of CdTe/MZO devices.[3] This study specifically examined the effects of MZO thickness and band gap (controlled by Mg/Zn ratio). Interestingly, this study observed a roll-under effect in JV measurements (similar to observations described in this report) in cases where the MZO layer was either too thin or had too high a band gap. The study also examined the effects of aging on work function of MZO films (not yet processed into devices) and observed changes on the order of 0.2 eV over a period of six months. The study concluded that MZO properties were relatively stable, but effects of stressing on device performance were not examined.

Module-level degradation modes and mechanisms are also attracting interest. For example, a recent NREL study used transmission electron microscopy (TEM) and energy dispersive x-ray spectroscopy (EDS) to examine degradation in CdTe minimodules following stressing by exposure to elevated temperatures and light.[4] Key findings included observation of Na migration from the soda-lime glass (SLG) substrates to the CdS layer; and the appearance of S- and O-rich regions within the CdTe absorber that were thought to act as lifetime-limiting recombination centers. Masuda et al. reported a comparative study of potential-induced degradation (PID) in superstrate CdTe vs. a-Si:H/μc-Si:H modules, both of which used a SnO_2:F front contact layer on glass substrates.[5] In this study, modules were subjected to bias voltages ranging from -2000 V to +500 V at elevated temperature (85 °C) and low relative humidity (< 2%). The study found that degradation modes and timescales were similar for the two types of modules and concluded that damage to the SnO_2:F TCO layer resulting from H_2O ingress caused the observed delamination and was the primary cause of performance loss.

5.2 Hybrid Perovskite Solar Cell Stability and Degradation

A recent study that compares degradation across several established and emerging PV technologies identified a broad range of degradation issues for hybrid perovskite solar cells.[1] The study identified cell-level issues, such as Au or Ag corrosion due to iodine migration, and electrode diffusion into charge-selective layers. Absorber degradation issues that were identified included decreases in absorption due to external stresses, migration of dopants from interlayers into the absorber layer, and phase separation such as PbI_2 formation that accompanies loss of the organic perovskite constituents. Another recent review of HPSC degradation highlights several degradation pathways for hybrid perovskite materials in the presence of H_2O or O_2.[6] This review also discusses thermal decomposition of hybrid perovskite material, using $CH_3NH_3PbI_3$ as an example, which results in PbI_2 formation accompanied by loss of organic constituents in the form of CH_3NH_2 and HI. A recent review by Khenkin et al. considers bias-dependent degradation (i.e., relative degradation rates and modes at various bias conditions, including short-circuit, maximum power point, and open-circuit conditions) in HPSC devices, and compares observations in various studies to known degradation modes and mechanisms in CdTe and CIGS solar cells.[7] The study concludes that a complex interplay exists in which multiple degradation mechanisms show bias dependence, including charging of light-generated traps, electromigration and diffusion of intrinsic and extrinsic ions, and radical formation in regions of high electron accumulation.

A recent review and perspective article on hybrid perovskite materials describes in detail key issues related to e-beam damage relevant to the application of CL (and by extension, other electron-probe based techniques including EBIC, TI, etc.) in hybrid perovskite materials.[8] This review highlights best practices for e-beam based measurements of hybrid perovskites, including: minimizing incident beam current; minimizing beam voltage (generally to below 10 kV); minimizing exposure time for any particular area of the sample to the electron beam; and performing electron-beam based measurements at temperatures near typical device operating temperature (to avoid phase transitions that can occur in hybrid perovskite materials at low temperatures). It should be noted that similar considerations apply to x-ray-based measurements such as XPS, particularly with respect to probe-beam flux and exposure times.

6 Project Objectives

This project developed approaches for studying performance limitations and degradation issues in PV devices that closely couple characterization with device modeling. Experimental tasks focused on development, validation, and application of a set of complementary characterization techniques and related sample preparation methods that combine surface characterization, electron- and scanning-probe-based microscopies, and optical spectroscopies, as well as in situ and operando capabilities. Physics-based device modeling was central to both rigorous interpretation of characterization results and understanding performance degradation in the PV devices that were studied.

The project was organized into six tasks. Four of these were tightly integrated tasks aimed at developing and validating novel characterization capabilities and physics-based computational models, and subsequently applying these to study degradation processes in Cd(Se,Te) and hybrid perovskite PV devices. A fifth experimental task was focused on dedicated electro-optical characterization of hybrid perovskite interfaces, and the sixth task was devoted to outreach activities in the form of peer-reviewed publications and conference presentations. The tasks are summarized below.

6.1 Task 1: PV Characterization Technique Development

This task developed novel characterization techniques, including in situ stressing and operando measurement capabilities, that enable correlative multi-mode experiments that track physical changes during cell-level degradation processes. Table I lists basic processes responsible for cell-level degradation mechanisms. Table II summarizes the key experimental approaches relevant to these degradation processes that have been developed and implemented to track the effects of stressing on material properties and device performance. These techniques have been applied to provide insights into effects of stressing on key device-physics processes illustrated in Figure 1 for baseline Cd(Se,Te) and hybrid perovskite PV devices. The correlative multi-mode approach coupled with device modeling in this project science enables deeper understanding of these processes, how they interact in real-world devices under operating conditions, and how they evolve over time in response to environmental stresses.

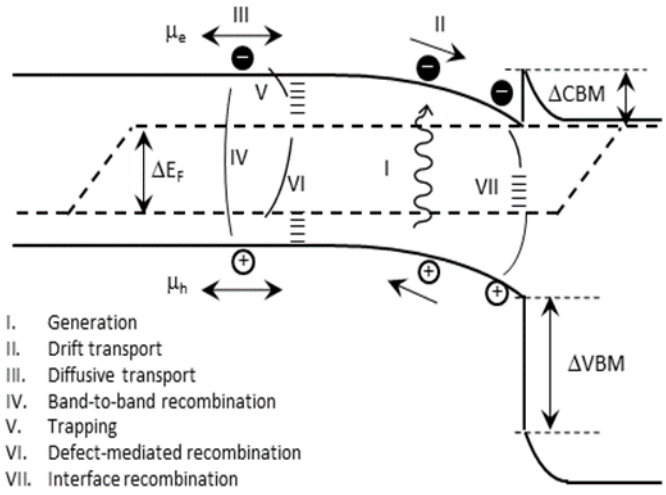

Figure 1. Schematic band diagram for a PV p/n junction showing interrelated carrier generation, transport, recombination, and collection processes.

Table I. Fundamental cell-level PV degradation processes and relevant environmental stress factors.

			Environmental stresses			
Degradation Process	Dimensionalities	Length Scales	T	V_{bias}	hν	Contaminants (e.g., Na^+, H_2O)
Point-defect equilibria	0D	1 – 10 nm	Temp.-controll X	X	X	X
Diffusion	1D–3D	100 nm – 1 μm	X			X

			Environmental stresses				
Degradation Process	Dimensionalities	Length Scales	T		V_{bias}	hν	Contaminants (e.g., Na^+, H_2O)
Electromigration	1D–3D	100 nm – 1 μm		X	X	X	X
Interfacial segregation	2D	1 – 10 nm		X			X
Secondary phases	0D–3D	10 nm – 50 nm		X			X
Material loss	0D–3D	100 nm – 1 μm		X			
Phase changes	3D	10 nm – 1 μm	T_c	X			

Table II. Overview of operando techniques with *in situ* stressing capabilities developed in the project and applied for multi-mode studies of PV degradation mechanisms.

Technique	Dimensionality/ Spatial Resolution	*In situ* Stresses	*Operando* Parameters	Physical Properties Measured	Insights Provided
popXPS	0D–2D 50 μm	T, hν, chemical	V_{OC}	composition, chemical states, valence band, and iDOS; pulsed light-bias provides information on V_{OC} transients	provides V_{OC} with concurrent interface properties; bandgap, defect states, recombination processes
CL, EBIC	2D 5 nm	T, V_{bias}, hν	J-V	carrier collection, luminescence intensity, and spectral character	carrier-recombination behavior, defect distributions, loss mechanisms
KPFM	2D 30 nm	T, V_{bias}, hν	J-V	electrical potential, photovoltage	potential across device stack, local V_{OC} fluctuation, potential inhomogeneity
sMIM	2D 50 nm	T, V_{bias}, hν	J-V	capacitance response	carrier concentration and type, ns–μs time resolution with ~50-nm resolution
TOF-SIMS	0D–3D 100 nm	--	--	secondary-ion signals	high-sensitivity composition, chemical information at 100-nm spatial resolution
TRPL	0D–3D 1 μm	--	J-V	photoluminescence decay	minority-carrier lifetimes, including bulk, GB, and interface recombination effects
TI	0D–3D 100 nm	--	--	luminescence intensity	coupled carrier diffusion-recombination effects, spatial variations in L_D

6.2 Task 2: Correlative Measurement and Device Model Development and Validation

The device modeling tasks in this project developed physics-based models using COMSOL Multiphysics® software, initially to describe performance in baseline (unstressed) Cd(Se,Te)/MZO and hybrid perovskite devices. These baseline device models were also used to rigorously simulate TI, EBIC, CL, KPFM, and popXPS measurements to provide accurate assessments of critical device physics parameters, including interfacial band offsets, carrier densities, electron affinities, interfacial defect densities, etc. The corresponding measurement simulations that were developed enabled direct correlations between those parameters and *operando* device performance metrics such as V_{OC}. A key goal met by the project was to use physical properties extracted from correlative measurements and measurement simulations to

constrain device physics models. Upon completing development and validation of these baseline modeling capabilities, the combined characterization plus modeling methodology was applied to track changes in device-physics parameters as a function of stress and identify material or device parameters responsible for performance degradation.

6.3 Task 3: Application to CdTe Solar-Cell Degradation Mechanisms

Results from this project complement ongoing efforts in the NREL CdTe core project to understand the role of as-processed interface properties in high-performance devices based on Cd(Se,Te)/MZO, and group-V doped CdTe absorber layers. Recent work at NREL on the use of Cd(Se,Te) alloys for bandgap grading, MZO emitter layers, and group-V dopants for improved doping characteristics, hold the promise of significantly higher device efficiencies. On the other hand, much remains to be discovered about potential degradation modes and metastabilities in devices that incorporate these novel approaches. In this project we documented stress-induced degradation modes and mechanisms in baseline Cd(Se,Te)/MZO devices provided by our collaborators (W.S. Sampath group, Colorado State University (CSU)).

Yearly Milestone Subtask 2.3.3: Demonstrated less than 20% deviation between simulated device parameters (V_{OC}, J_{SC}, FF, PCE) and actual measured performance of stressed baseline Cd(Se,Te)/MZO devices, using model input parameters derived from correlative TI, CL/EBIC, TRPL, opXPS, KPFM and sMIM measurements.

6.4 Task 4: Application to Hybrid Perovskite Solar-Cell Degradation Mechanisms

Results from task 4 studies complement ongoing efforts in the NREL hybrid perovskite core project and industry partners to optimize materials and interfaces with respect to performance and stability. Hybrid-perovskite materials are known to be very sensitive to damage from electron and x-ray radiation, making reliable SEM- or XPS-based measurements challenging. To mitigate these issues, we performed baseline TI and XPS measurements on hybrid perovskite materials and devices to quantify the extent of damage, and subsequently developed variations on these techniques that use alternative excitation sources including optically excited TO (o-TI), and pulsed light-bias operando ultraviolet photoelectron spectroscopy (popUPS).

Yearly Milestone Subtask 3.4.3: Publication identifying degradation mechanism(s) based on findings from 4.1, 4.2, 4.3, specifically, addressing whether interfacial degradation is still a limiting factor, or if degradation of the bulk absorber now dominates.

6.5 Task 5: Correlative EO and Chemical Analysis for Buried Hybrid Perovskite Interfaces

Increase in efficiency and reliability of hybrid perovskite PV is necessary for TW-scale, carbon-neutral electricity generation. Efficiency losses increase PV costs and can make technology less competitive. Most losses in solar cells are attributed to charge carrier recombination, which can occur in the semiconductor absorber bulk and at device interfaces. In task 5, we developed electro-optical (EO) methods to quantify voltage

losses in hybrid perovskite solar cells. Such analysis is needed for hybrid perovskite PV R&D and for metrology. Special focus was applied to quantify and understand losses at device interfaces, because interface recombination is the current bottleneck of hybrid perovskite PV. For more advanced architectures (tandems, all-back-contact cells, etc.) interfaces increase in complexity, making this characterization effort timely. This task has met three annual milestones, which were to “develop hybrid perovskite interface recombination analysis capability based on TRPL spectroscopy (1.5.1)”, “apply and validate interface and bulk V_{OC}-loss analysis to hybrid perovskites with different electron and hole transport layers (2.5.1)”, and “apply and validate interface and bulk V_{OC}-loss analysis to hybrid perovskites with variable bandgaps (3.5.1)”. As described in milestones, analysis was developed and validated for several hybrid perovskite solar cell architectures and compositions. Specific examples are given in Project Results and Discussion section.

6.6 Task 6: Publications and Outreach

Publications and conference presentations are summarized in Section 11 of this report.

7 Project Results and Discussion

7.1 Task 1. PV Characterization Technique Development

The following subtasks both relate to development and validation of sample preparation techniques for electron-beam-based measurements and are discussed together.

7.1.1 Subtask 1.1.1: Development of bevel-fabrication procedures for CdTe films and devices for cross-sectional transport imaging analysis, where RMS surface roughness measured by AFM is <100 nm roughness. The yield of successful samples is expected to be 90% or higher.

7.1.2 Subtask 1.1.4: Development of polishing and ion milling procedures for the fabrication of cross sections of CdTe samples and devices suitable for transport imaging analysis, as indicated by more than 90% of pixels having better than 95% confidence index in EBSD map.

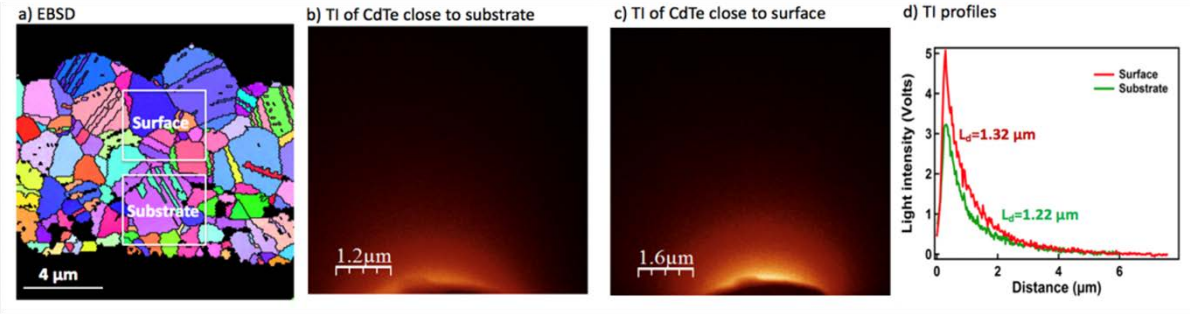

Figure 2. (a) EBSD and (b)-(d) TI data from two locations on a beveled sample prepared on the SEM-FIB.

Experimental techniques that were extensively employed in the project for studying electro-optical properties of PV devices, including TI, KPFM, and EBIC, relied on sample preparation methods for creating extremely high-quality bevel and cross-section samples. In this context, sample quality was assessed primarily through a combination of surface roughness (assessed by atomic force microscopy (AFM)) and surface crystallinity (assessed by electron backscatter diffraction (EBSD)). Three approaches were explored for preparing cross-sectional and beveled samples:

- **Dimpler**: The dimpler is a polishing device in which the polishing wheel rotates on a horizontal axis in contact with the sample surface as the sample rotates on a vertical axis. Dimpler parameters were optimized for samples with different thicknesses, from several dozens of microns to <3 μm. After dimpling, Cd(Se,Te) samples were etched with bromine/methanol solution or ion milled to create a highly crystalline surface.
- **Mechanical polishing**: Polishing using a diamond pad with particle sizes down to 50 nm and finally colloidal silica was found to create flat beveled surfaces with < 50 nm corrugation over ~30 μm-wide areas. The beveled samples were made using sample holders with bevel angles of 5° (surface area 10x larger), 10° (5x), 20° (3x), and 45° (1.5x).
- **SEM-FIB**: In this method the sample is positioned at a given angle from the ion beam and a trench is milled, creating the bevel. FIB trenching is very time consuming but can create high-quality bevels and cross-sections on thin (few-μm - thick) samples.

In general, the mechanical polishing approaches required an additional ion milling step to remove a surface-damage layer. Each of the three preparation methods listed above created surfaces with roughness < 100 nm, and with excellent crystallinity, as demonstrated by EBSD orientation maps with more than 90% of pixels having better than 95% confidence index. A noteworthy result was that the dimpler procedure was able to create an 800-μm-wide bevel on a 2.8-μm thick sample, an increase on the exposed cross section of about 285x. Figure 2 shows initial EBSD and TI analyses on a CdTe layer at two different depths, on a bevel sample created in the SEM-FIB. The EBSD image highlights the excellent crystalline quality of the bevel surface. The TI measurements reveal higher luminescence and a slightly longer diffusion length on the region close to the surface. These effects are likely associated with higher surface recombination rates at the CdTe/substrate interface, coupled with a higher degree of grain-boundary recombination associated with the finer grained-material near the substrate.

7.1.3 Subtask 1.1.2: Development of pulsed light-bias opXPS capability is able to measure <20 ns minority-carrier lifetimes and agrees with TRPL measurements within a factor of 2.

Figure 3 illustrates the basic concepts underlying the pulsed-light-bias operando XPS approach. DC light bias results produces a shift in XPS core levels relative to the no-light-bias case due to open-circuit voltage across the PV device (red vs. yellow XPS spectra). For the slow-pulse case, the photovoltage decay transient is fast relative to the

light-bias pulse period, such that the measured XPS spectrum (green) is the average of the no-light-bias and DC light bias cases. At the other extreme, the pulse frequency is sufficiently fast that carriers in the device do not have time to decay between pulses, so that the XPS peak shape converges to that of the DC light bias case. At intermediate pulse frequencies, the photovoltage decay transient occurs over a timescale similar to the pulse period, so the XPS peak takes on an intermediate line shape (blue XPS spectrum) that averages over the constantly changing photovoltage.

A pulsed diode laser with a fast-gating capability was used as the light source for the popXPS technique. The laser was operated at its highest pulse frequency (100 MHz) while square-wave gating pulses were applied at frequencies over the range 1 Hz to 10 MHz. This approach produced pulse trains capable of high temporal resolution (on/off response <1 ns) as well as constant average light intensity. Thus, the system was capable of measuring photovoltage decay transient responses down to 20 ns. But in general, over the course of the project, popXPS measurements on PV devices found typical photovoltage decay timescales were always substantially longer than 20 ns,

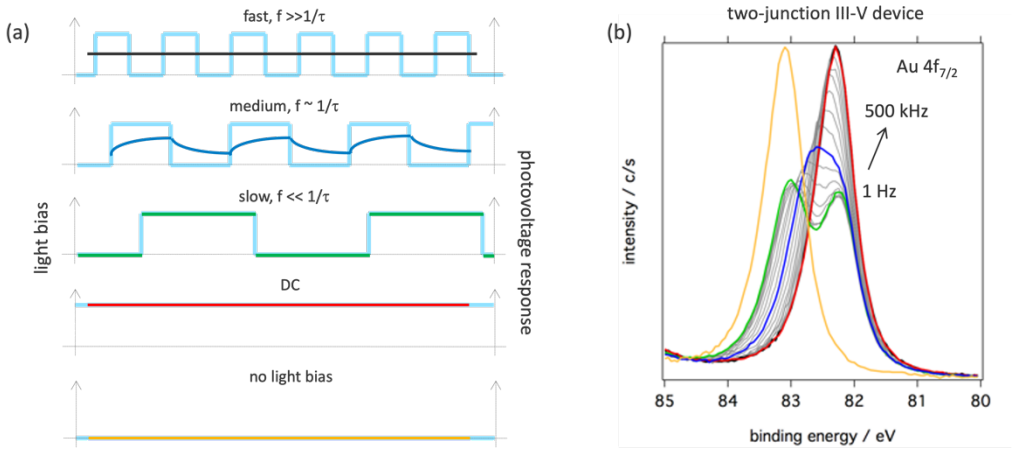

Figure 3. (a) Schematic illustration of the pulsed-light-bias operando XPS (popXPS). (b) Example popXPS data set acquired on a tandem III-V solar cell.

primarily because photovoltage decay measurements are sensitive to much lower minority-carrier concentrations, which persist over much longer times, than techniques like time-resolved photoluminescence.

7.1.4 Subtask 1.1.3: Development of light (0 to 1 sun) and voltage (± 2 V) bias capabilities for CL/EBIC analysis, as verified by comparison with J-V data from devices measured on a standard test system such that J_{SC} and V_{OC} values agree within 10%.

This task demonstrated a capability to measure EBIC signal variations at grain boundaries and interiors (GBs and GIs) in PV device cross-sections under applied voltage and light bias. A custom scanning electron microscopy (SEM) sample stage that enables the sample to be contacted, and voltage and light bias applied, was designed

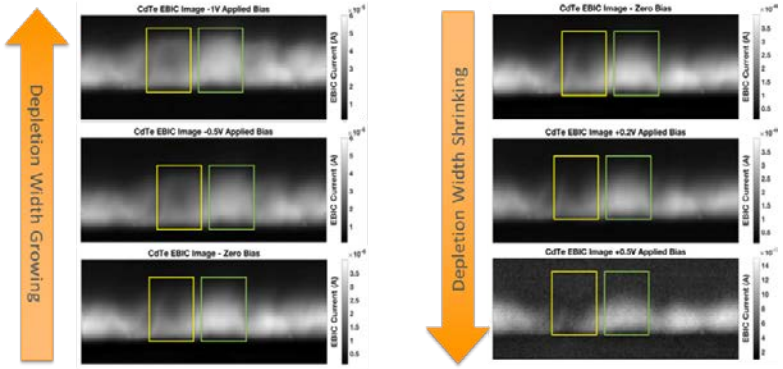

Figure 4. Cross-sectional EBIC images of a CdTe sample in the superstrate configuration (junction at bottom of image) acquired under applied voltage bias using a lock-in amplifier and pulsed electron beam. The collection profile can be seen to grow (reverse bias) and shrink (forward bias) based on the depletion region response to the bias voltage value.

and fabricated. Due to the large DC currents present when applying combinations of voltage and light bias to devices with areas up to ~1 cm^2, a lock-in amplification scheme was implemented to reduce noise and improve image quality in these experiments. Examples of high-quality EBIC images are shown in Figure 4 for a CdTe device in cross-section. The collection profiles clearly change with applied voltage bias as seen in the yellow and green rectangles. The collection profile can be seen to grow (reverse bias) and shrink (forward bias) based on the depletion region response to the bias voltage value. EBIC line scans, with and without lock-in detection, across a CdTe grain boundary are shown in Figure 5 (a). A small offset is present in the measurement made using the lock-in system which is attributed to a “beam sweeping” phenomenon that occurs when operating the beam blanker at the upper end of the allowed frequency range. Alternative beam blanking systems are being investigated to address this issue.

The operando capability of the EBIC system was demonstrated by measuring J-V curves within the SEM chamber. In Figure 5 (b) the black curve represents a reference measurement made on a standard solar simulator, while the blue curve is produced under illumination in the SEM chamber. The slight discrepancy in open-circuit voltage (V_{OC}) is likely due to sample heating. Within the SEM vacuum chamber there is no ambient to conduct heat way from the sample surface so heating under illumination is more pronounced.

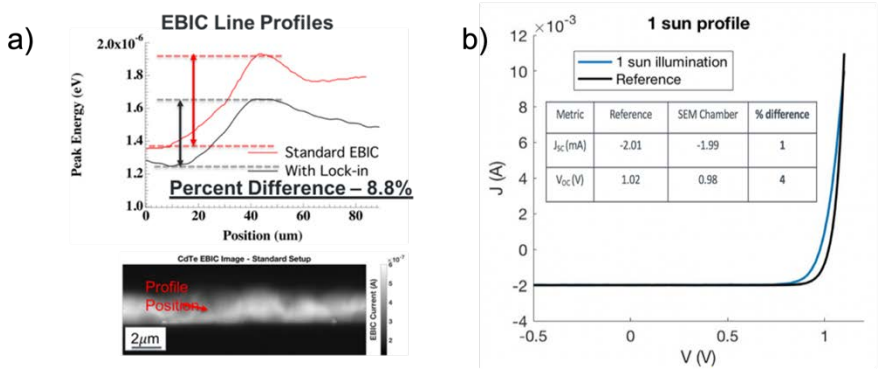

Figure 5. a) EBIC line profiles across a grain boundary (shown in EBIC image) for the standard EBIC setup (red) and using the lock-in amplifier and pulsed electron beam (black). b) Illuminated J-V characteristics of a GaAs device taken outside the SEM chamber on a standard measurement setup (reference curve) and within the SEM chamber where illumination via a solar simulator directed through an optical port.

7.1.5 Subtask 1.1.5: Development of in situ stressing and operando plan-view nanoelectrical probes (KPFM/SCM/SSRM) with sample drift less than 10 nm/min (15 mm/day) for stress conditions of 85 ˚C and 1-sun light bias.

This subtask developed upgraded atomic force microscopy (AFM) capabilities encompassing three main techniques, including: (1) Kelvin probe force microscopy (KPFM) (electrical potential mapping with ~30 nm spatial and ~10 mV electrical resolutions, respectively); (2) scanning spreading resistance microscopy (SSRM) (resistivity mapping with ~10 nm resolution); and (3) scanning capacitance microscopy (SCM) (carrier concentration mapping with ~20 nm resolution). A sample platform that includes thermal (25 ˚C to 85 ˚C), light-bias (up to 1 sun), and high voltage (up to 1kV) stressing capabilities was developed for existing AFM instruments configured for KPFM, SSRM, and SCM nanoelectrical imaging modes. The compact design of the in situ stressing platform (Figure 1) integrates all three stressing parameters (T, light bias, V). The circular symmetry of the design, with the sample mounted at the center, minimizes thermal drift. The limited space available in our existing AFMs requires a compact design, but the low thermal mass also benefits experiments requiring rapid temperature changes.

Performance metrics for the AFM-based in situ stressing platform were tested on an ion-mill polished thin film CdTe device sample. For the thermal drift test, particulate features were identified on the surface to track lateral motion. Figure 6 (a)-(b) shows a drift measurement at 85 ˚C, where vertical and lateral drifts of 410 nm and 170 nm, respectively, in 80 min equate to a net a drift of 6 nm/min, exceeding the 10 nm/min

performance metric, and demonstrating an ability to track specific sample areas over long periods.

Figure 6 (c) shows a KPFM image acquired on the CdTe film with 1 kV bias voltage toggled during imaging. No signal disturbances were observed, due to the well shielded sample cover and the separate ground connections provided for the cover, the high voltage source, and the AFM instrument. Figure 6 (d) shows a KPFM image with 1-sun light-bias toggled on and off. With illumination, the overall potential increases by the device V_{OC}, but here were no observable changes in noise level or image quality. Additional KPFM imaging tests were conducted at 85 °C with various combinations of the other stress factors, and no significant increases were observed in noise levels. Thus, the design, installation, and testing of our in situ stressing capability met or exceeded all performance metrics.

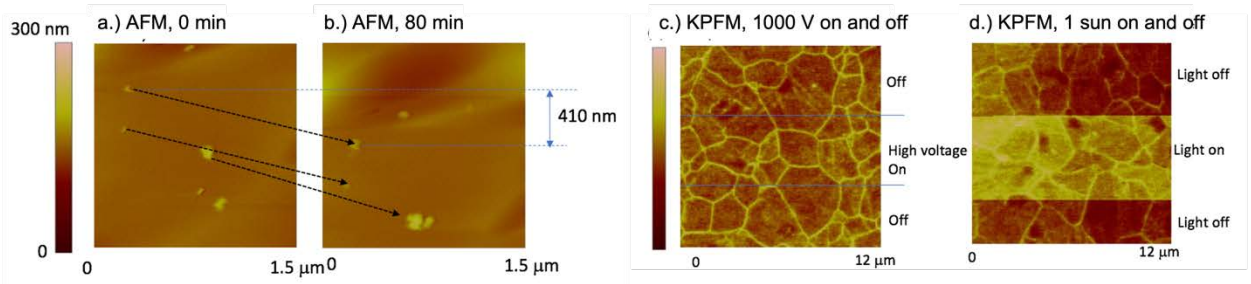

Figure 6. AFM images taken at (a) 85 °C at 0 min and (b) 80 min, illustrating the extent of thermal drift. KPFM images taken with (c) the high voltage and (d) the illumination turned on and off, illustrating no observable increase in noise level by the stressing.

7.1.6 Subtask 1.1.6: Developed light-biased sMIM capability with spatial resolution below 100 nm and ability to measure minority-carrier lifetimes down to τ >= 5 ns:

In partnership with NIST Boulder, this project developed and validated an optically excited sMIM capability that met two key performance metrics, including (1) spatial resolution better than 100 nm, and (2) measured carrier lifetimes within a factor of 2 of lifetimes measured by conventional time-resolved microwave conductivity (TRMC) or time-resolved photoluminescence (TRPL). Our base MIM instrument is a heavily modified commercial tool that sources its signal from a vector network analyzer and detection is accomplished via I/Q mixer-based detection [9] that enables high bandwidth detection as desired for time-domain measurements. Spectrally continuously tunable pulsed excitation is provided by amplitude shaping the output of a pulsed broadband supercontinuum laser [Figure 7 (a)] and is delivered to the sample from below [Figure 7 (b)]. The MIM is sensitive to the tip-sample admittance Y_S [Figure 7 (b)], which directly reflects the local free carrier concentration. A MIM time-domain trace obtained from a MC hybrid perovskite thin film is compared with TRMC and TRPL obtained from identical sibling samples [Figure 7 (c)], which reveals agreement with TRMC well within a factor of 2. Furthermore, the difference between the microwave techniques and the TRPL directly arises from the distinct mechanisms used, in which the PL signal arises

from bimolecular recombination whereas the microwave-impedance-based methods are sensitive to the holes and electrons independently.

7.2 Task 2: Development PV Device Models

The general approach to modeling the baseline Cd(Se,Te) and hybrid perovskite PV devices in this project involves solving the fundamental semiconductor device equations using the finite element method with COMSOL Multiphysics® software.[10] We developed customized physics-based simulations to emulate various characterization techniques (including popXPS, TI, CL, EBIC, TRPL, and KPFM potential profiling), in addition to predicting performance under standard conditions. These device models

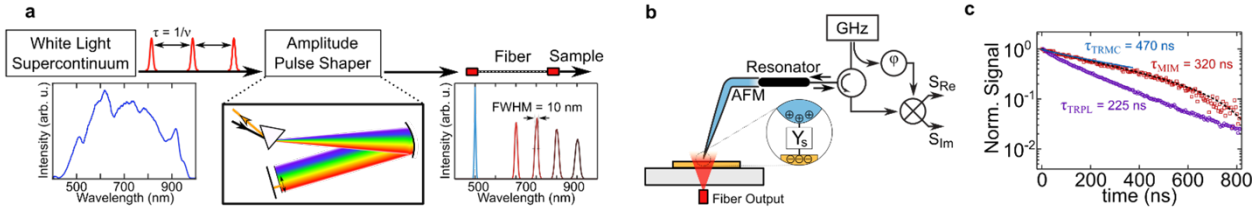

Figure 7. (a) A supercontinuum source provides continuously spectrally tunable pulsed optical excitation that is used to photoexcite carriers in the sample that (b) are detected using sMIM via the tip-sample admittance, Y_S. (c) Time domain MIM traces from a hybrid perovskite film are compared with TRMC and TRPL obtained from sibling samples.

were validated by comparing model results to measured performance metrics and characterization data. The multi-mode characterization and modeling approach provided unique insights to device properties and important degradation features, as described below.

This task developed and validated 1D–3D device-physics models using the COMSOL platform to describe performance of the unstressed baseline Cd(Se,Te)/MZO and hybrid perovskite devices studied in this project. Variations of these baseline device physics models were also configured to simulate TI, EBIC, CL, KPFM, and popXPS measurements, providing a means for assessing key device-physics parameters. A key goal of these measurement simulations is to use physical properties extracted from correlative measurements on standardized device structures to constrain device physics models.

7.2.1 Subtask 1.2.1: Demonstration of baseline 1D, 2D, and 3D Cd(Se,Te)/MZO and hybrid perovskite/C60/SnO_x/Al device models, where performance metrics (V_{OC}, J_{SC}, FF, Eff.) obtained from COMSOL vs. baseline models agree within 5%.

Prior to studying devices specific to this project, baseline device models were built and benchmarked to replicate published data for hybrid perovskite [11] and Cd(Se,Te)/MZO [12] devices. Models developed in COMSOL were also tested by comparison to equivalent models in the SCAPS software package [13]. We achieved better than 5% agreement between the COMSOL and SCAPS device performance parameters, J_{SC}, V_{OC}, FF, and efficiency. Good agreement was also achieved with the published data. Details on the devices studied in this work are provided in subsequent sections of this report.

7.2.2 Subtask 1.2.2: 3D Transport Imaging (TI) models developed in COMSOL for (1) cross-sectional measurements with spot-mode excitation perpendicular to a p-n junction and (2) plan-view measurements with line-mode excitation perpendicular to a GB.

TI models were developed in COMSOL and applied to Cd(Se,Te)/MZO devices for comparison to measurements. These models required simulation of e-beam excitation in the absorber material. Figure 8 (a) shows the cylindrical electron-hole pair generation volume created by an e-beam that is being scanned in and out of the page. These calculations simulate TI measurement conditions for 1 nA beam current with 20 keV energy. The simulated e-beam excitation was translated across the device cross section and the radiative recombination rate was calculated as a function of distance from the back contact for each beam location. Based on published data for a similar device [12] and our own measurements, the Cd(Se,Te) layer had a graded band gap from 1.5 eV near the back of the device (CdTe) to 1.39 eV ($CdSe_{0.16}Te_{0.84}$) [14] within about 1 μm from the MZO layer. For simplicity, the initial model had a linearly graded bandgap between the CdTe and $CdSe_{0.16}Te_{0.84}$, as shown by the blue line in Figure 8 (b). Electron affinity of the Cd(Se,Te) layer was varied in direct proportion to the bandgap grading.

For unstressed Cd(Se,Te) devices, an anomalous double peak was observed in TI measurements when the e-beam was in certain locations (a single peak, near the e-beam excitation, is typically expected). This double-peak structure was not observed in stressed devices. Our simulations indicated that the anomalous second peak occurred near the minimum of the graded Cd(Se,Te) band gap (~2.6 micron from the back contact). To investigate further, the band gap grading within the model was varied using a smoothing parameter (*s*) which determined the length of the transition zone between the high (1.50 eV) and low (1.39 eV) band gap regions. Bandgap smoothing of $s = 0.8$ and $s = 2.4$ are shown in Figure 8 (b). Figure 8 (c) shows that the JV curve is not noticeably affected by changes in band gap smoothing alone, while Figures 8 (d-f) show that the second peak disappears as the grading becomes smoother. Therefore, band gap smoothing can explain the TI double peak, but it does not appear to be associated with the observed degradation mode (discussed in Section 7.3) of excessive FF loss. Band gap smoothing could be caused by Se diffusion during stress, which is corroborated by EDS measurements (not shown).

While the relevant qualitative features of the TI data were captured by the models and interesting carrier transport phenomena were revealed, direct quantitative comparisons were not possible because absolute values of emitted light intensity were not available from the TI measurements. On the other hand, the carrier diffusion length implied by the experiments and models agree on a value of approximately 2 μm.

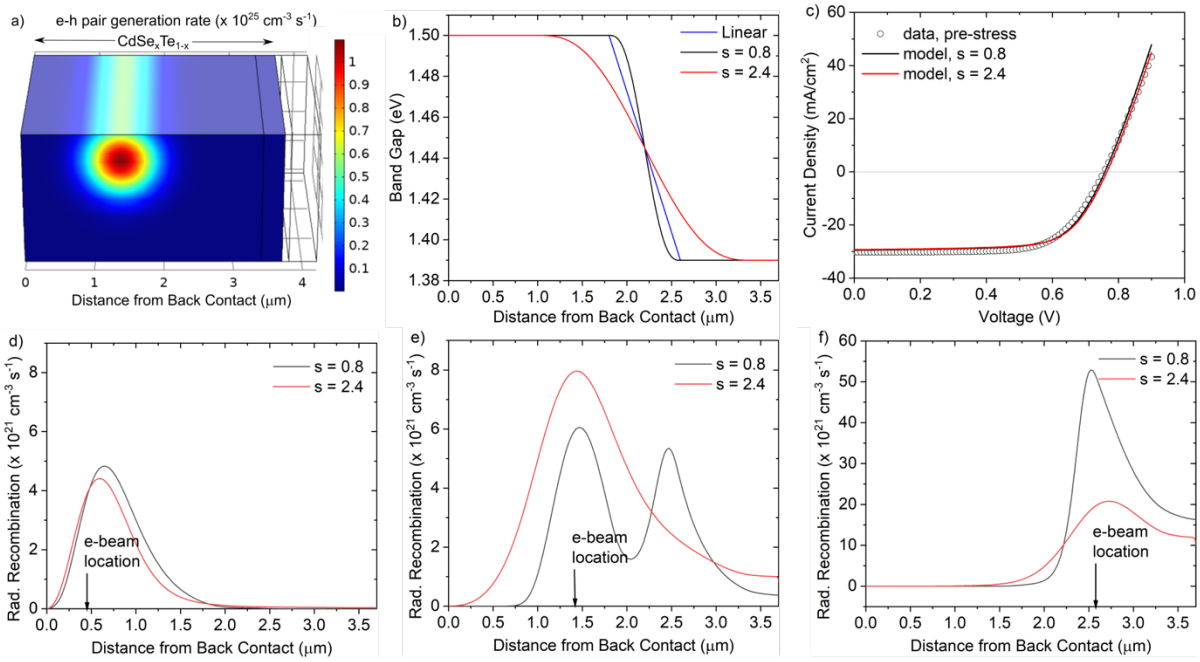

Figure 8. Simulated e-h pair generation volume due to e-beam excitation (color plot) in the Cd(Se,Te) layer. (b) Band gap grading profile of Cd(Se,Te) showing linear case and two smoothing parameters s = 0.8 and s = 2.4. (c) JV data (for unstressed Cd(Se,Te) device compared to models with s = 0.8 and 2.4. (d) – (f) simulated TI response for the three e-beam locations indicated at s = 0.8 and 2.4. The characteristic double peak is evident for the steeper band gap gradient.

7.2.3 Subtask 2.2.1: Demonstration of 3D measurement simulation models for CL/EBIC, KPFM, and popXPS, where measured and simulated experiment signals agree within an overall factor of 2.

COMSOL device models were developed to simulate CL/EBIC with e-beam excitation, similar to TI models described in the previous section. CL signals are simulated by integrating the radiative recombination rate over the volume of the device (total light emitted); and EBIC requires calculating the total collected current. Pulsed-light excitation capability was also developed to simulate the transient photovoltages probed in popXPS measurements. Simulation of KPFM potential profiles did not require the simulation of novel excitation sources in the models; rather, it involved comparing the calculated built-in electric field under equilibrium conditions to the KPFM results. These simulation tools and results are described in turn below.

CL and EBIC simulations were applied to both pre- and post-stress Cd(Se,Te) devices. The differences between pre- and post-stress model parameters are provided in Task 3 below. The aforementioned stress-induced change in band gap smoothing was also accounted for in these simulations. The CL calculations in Figure 9 (a) indicate that the CL signal is stronger in the Se-rich region where the band gap is smaller. Furthermore, the stressed device exhibits slightly lower CL signal, suggesting a reduction in carrier lifetime with stress. These results are in qualitative agreement with the data. The overall shapes of the EBIC signals and significant reduction of current collection after stress,

shown in Figures 9 (b) and (c), are also consistent with observations for unstressed and stressed devices.

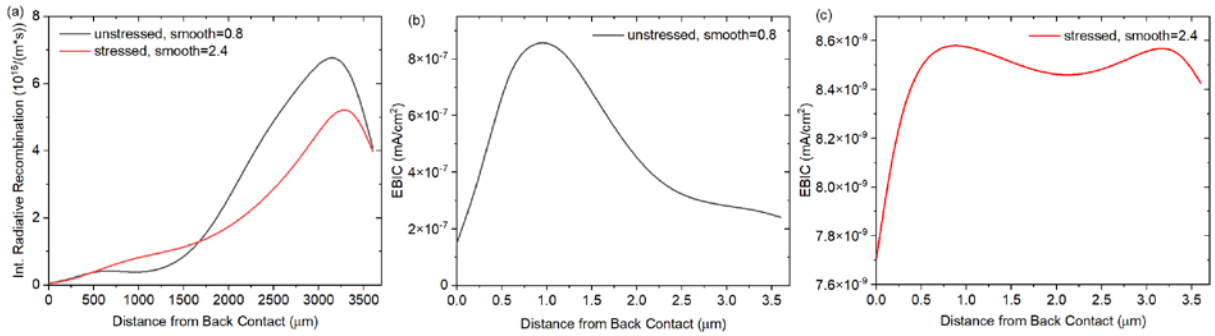

Figure 9. (a) CL calculations for unstressed and stressed Cd(Se,Te) device models including the band gap smoothing parameters discussed under Subtask 1.2.1. (b) and (c) EBIC calculations for unstressed and stressed devices, respectively (note the difference in ordinate scale).

PopXPS simulations were initially tested and applied to CIGS/CdS test structures, and subsequently further developed for Cd(Se,Te)/MZO devices with various buffer layer (MZO) thicknesses. Transient device photovoltages were calculated under visible light excitation over a broad range of pulse frequencies. As in the popXPS measurement experiments, a constant background excitation was included with intensity ~ 10^{-5} – 10^{-3} suns to account for photoexcitation by the x-ray source. Analysis of the measured and simulated popXPS data sets led to several important insights: (i) the binding energy (BE) shift observed as a function of pulsed-light frequency is directly correlated with the photovoltage decay transient that occurs during the off period of the light pulses; (ii) characteristic photovoltage decay times are on the order of 10s of μs (much greater than carrier lifetimes); and (iii) accurate data interpretation requires knowledge of the background X-ray intensity and its effect on minority-carrier populations in the device.

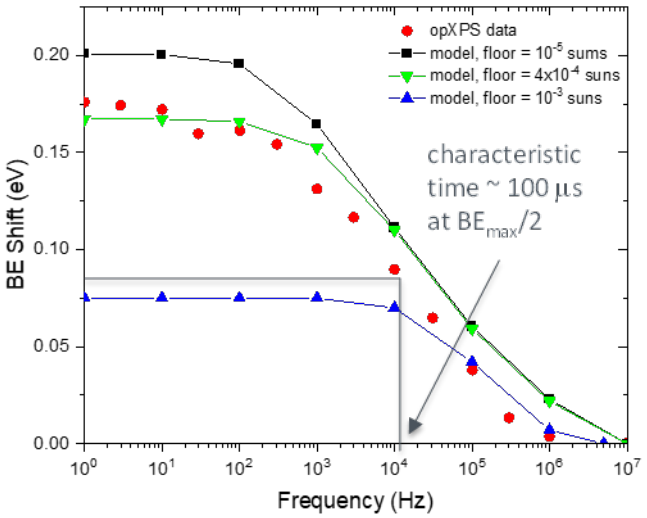

Figure 10. Cd(Se,Te)/MZO device binding energy shift measured with pulsed-light popXPS (circles) compared to simulation results at various background X-ray (floor) intensities. The characteristic time is defined as the inverse of the frequency at half the BE shift maximum.

Figure 10 shows measured and simulated BE shift data as a function of pulse frequency (circles) for popXPS measurements on a Cd(Se,Te)/MZO device. From the experimental data, a characteristic frequency (where BE shift is half the maximum observed value) ~10^4 Hz is observed. The inverse of the characteristic frequency yields a characteristic photovoltage decay time ~ 100 μs. Simulation results are shown in Figure 10 for three different background intensity (floor) values, indicating that a floor value of $4x10^{-4}$ suns most closely aligns with the data**.** We have demonstrated that pulsed-light popXPS provides a contactless method to probe carrier lifetime, mobility, and doping. Deconvoluting and extracting those variables from the data is the subject of future work.

7.3 Task 3: Application to CdTe Solar-Cell Degradation Mechanisms

This task applied novel characterization techniques, including in situ stressing and operando approaches, to understand degradation modes in baseline Cd(Se,Te)/MZO devices and identify dominant degradation mechanisms. Cd(Se,Te) devices studied in this project were provided through a collaboration with the W.S. Sampath group at Colorado State University (CSU). The architecture of these devices, illustrated in Figure 11 (a), were based on a bilayer CdTe/Cd(Se,Te) absorber with a $Mg_xZn_{(1-x)}O$ (MZO) emitter layer.

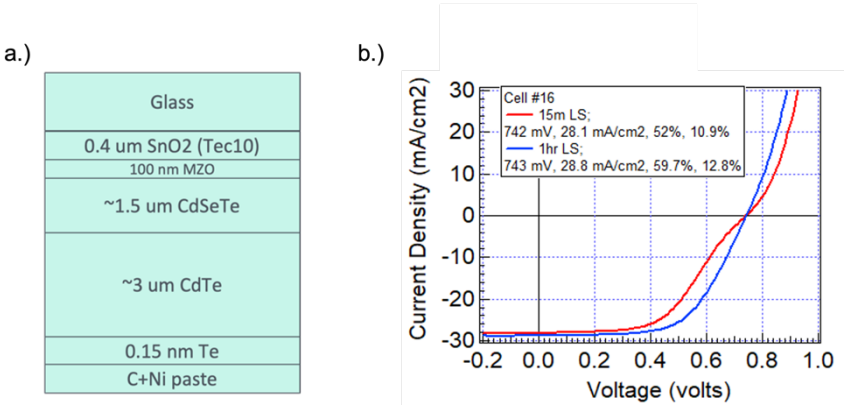

Figure 11. (a) Schematic of the standard CSU Cd(Se,Te)/MZO device architecture. (b) Illustration of "dark storage" metastability observed in the studied Cd(Se,Te)/MZO devices. Performance losses under storage conditions could be recovered via light soaking.

These baseline devices exhibited a pronounced performance metastability, where device efficiency decreased significantly under dark storage conditions, as shown in Figure 11 (b). This performance metastability primarily impacted fill factor in the device and could be reversed via light soaking. As will be discussed in more detail, the observed metastability had a similar effect on device performance metrics to the irreversible degradation modes that were the primary object of study. Consequently, a light-soaking step was incorporated into device characterization and measurement protocols.

7.3.1 Subtask 2.3.1: Documented cell-level degradation modes in baseline Cd(Se,Te)/MZO devices with initial performance in the 15-18% efficiency range that track changes in device parameters (V_{OC}, J_{SC}, FF, PCE) vs. time.

A set of Cd(Se,Te) devices were stress tested for 683 hours under 1-sun illumination at 65 °C. As summarized in Figure 12 (a), losses were observed in open-circuit voltage (V_{OC}) and short-circuit current (J_{SC}), the dominant degradation mode was characterized by a pronounced loss in fill factor (FF) associated with a so-called “roll-under” effect in the J-V curves.

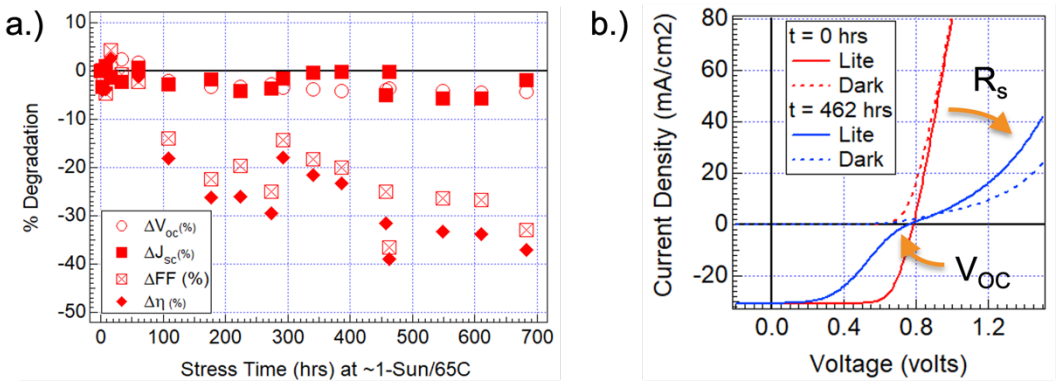

Figure 12. Plot showing performance degradation during stress testing of CSU Cd(Se,Te)/MZO solar cells. Most of the performance loss is due to decrease in fill factor associated with observed "roll-under".

Figure 13 summarizes results of capacitance-voltage measurements showing an increase in depletion width and decrease in majority-carrier density during stress testing.

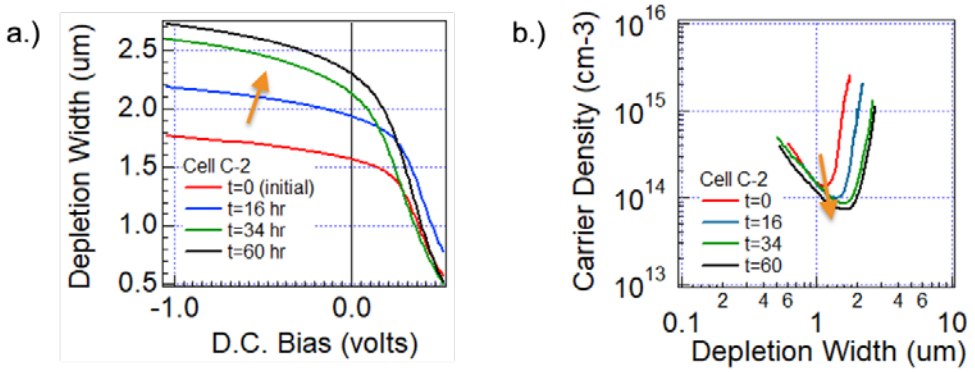

Figure 13. Degradation-induced changes including a.) increase in depletion width and b.) decrease in carrier density.

7.3.2 Characterization of Unstressed and Stressed Cd(Se,Te)/MZO Devices

KPFM Measurements on Stressed vs. Unstressed Cd(Se,Te)/MZO Devices:

The Cd(Se,Te) devices studied in this project displayed a pronounced performance metastability characterized by a loss in fill factor when stored in the dark that was reversible with light soaking. These devices also showed irreversible degradation when stressed under light-bias at elevated temperature (1 sun, 65 °C). Changes in electric potential profiles accompanying both the reversible and irreversible transitions within these devices were investigated using KPFM.[15] These measurements were performed on both unstressed (dark-soaked and light-soaked) and stressed (light-soaked) Cd(Se,Te) device samples to quantify changes in electric potential/field distributions that accompanied various stress conditions. Figure 14 shows KPFM-based potential images taken on an unstressed (light-soaked) device cross-section at various reverse bias voltages (0 to -1.5 V). As expected, the overall potential within the Cd(Se,Te) absorber decreases from the TCO layer toward the back contact. The potential images also show higher contrast at the grain boundaries (GB), indicating that the GBs are positively charged.[16] To quantify the potential distribution across devices, potential images were averaged over the y-axis to generate corresponding potential profiles spanning the x-axis. As has been described is previous studies [17],[18], the effects of charging (or band bending) related to the exposed cross-section surfaces were removed by subtracting the potential for the unbiased case from those with bias.

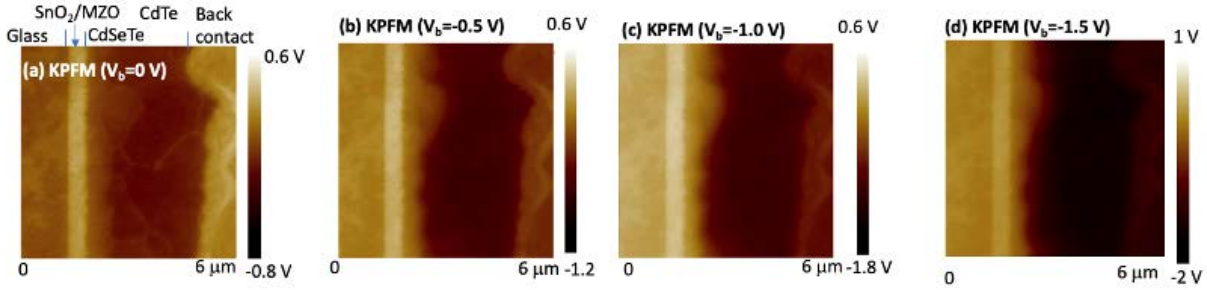

Figure 14. KPFM potential images taken on the cross-section of a Cd(Se,Te) device in the unstressed (light-soaked) state with various reverse bias voltages from V_b = 0 to V_b = -1.5 V.

The calculated electric field profiles then correspond to the first derivatives of the baseline-corrected potential profiles. In this manner it is possible to map electric field profiles within devices with spatial resolutions down to ~30 nm.

As shown in Figures 15 (a)(b)(c), for the unstressed (light-soaked) case the electric field exhibits a main peak within the Cd(Se,Te) layer, as opposed to at the MZO/Cd(Se,Te) heterointerface, consistent with the existence of a buried homojunction (BHJ) within the device. KPFM measurements on the unstressed (dark-soaked) case shown in Figures 15 (d)(e)(f) reveal that a significant second electric field peak has developed at the MZO/Cd(Se,Te) interface. As shown in Figure 15 (g)(h)(i), stressing (1 sun, 65 °C) produced an irreversible increase in the electric field peak at the MZO/Cd(Se,Te) interface. As will be discussed in more detail in subsequent sections, these results are consistent with popXPS measurements of the MZO/Cd(Se,Te) interface and device modeling results, suggesting that stressing results in an increase of the conduction

band offset spike at the MZO/Cd(Se,Te) interface, accompanied by some combination of a decrease in MZO n-type doping and/or an increase MZO/Cd(Se,Te) acceptor-type interface defect density.

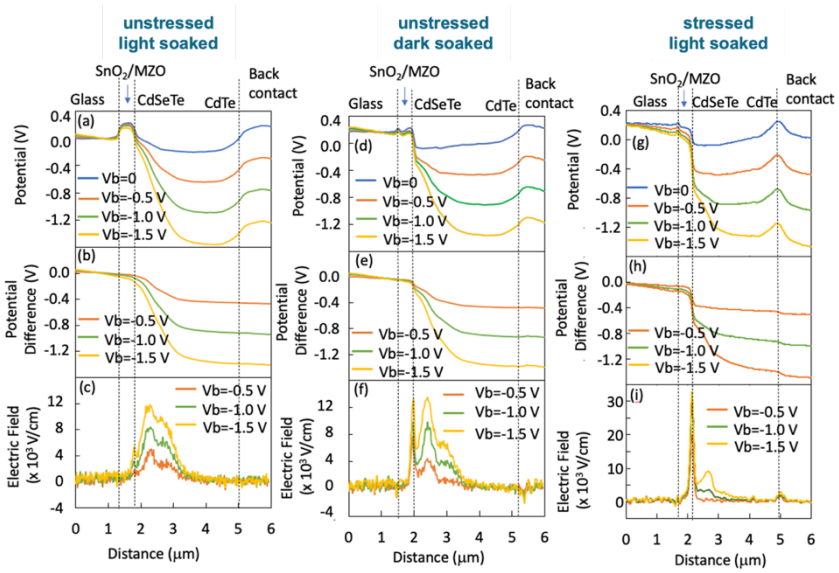

Figure 15. (a)(d)(g) Potential profiles measured with KPFM as a function of bias voltage (V_b); (b)(e)(h) calculated changes in potential profile relative to the V_b = 0 V case; and the corresponding electric field profiles for the (c) unstressed light-soaked, (f) unstressed dark-soaked, and (i) stressed light-soaked (degraded) states, respectively.

Pulsed Light Bias Operando XPS Measurements on Stressed vs. Unstressed Cd(Se,Te)/MZO Devices:

XPS is a powerful technique for studying materials and devices that provides information on composition, chemical states, and interfacial energy-band alignments. The addition of pulsed light bias further enables measurements that probe photovoltage decay transient phenomena. A strength of XPS is its short information depth, based on limited photoelectron escape depths, typically in the range 5–10 nm. On the other hand, the limited XPS information depth poses challenges in studies of buried interfaces, such as the MZO/Cd(Se,Te) interface. In the present study, a method was developed for exposing the MZO/Cd(Se,Te) interface, based on a sacrificial C60 layer, as illustrated in Figure 16. In this approach, the C60 layer is thin enough (~10 nm) that device performance is only slightly affected by light absorption or increased series resistance. At the same time, the standard MZO thickness in the CSU devices in this study was ~ 100 nm, still substantially beyond the XPS information depth, and therefore Ar^+-ion etching was employed to reduce the MZO layer thickness sufficiently to reveal the junction. Control popXPS measurements were performed to verify that Ar^+-ion etching did not damage the interface.

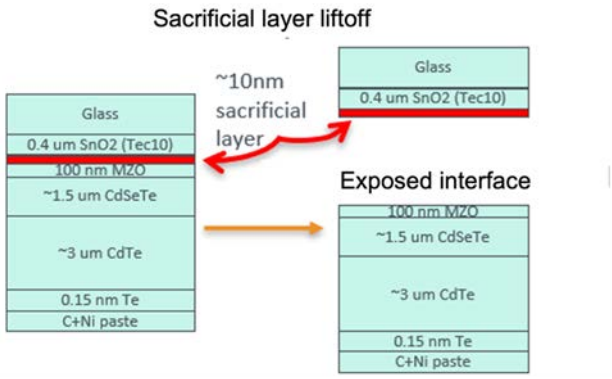

Figure 16. Schematic diagram illustrating the standard CSU Cd(Se,Te) device architecture and method for delaminating the active layers using a sacrificial C60 interlayer.

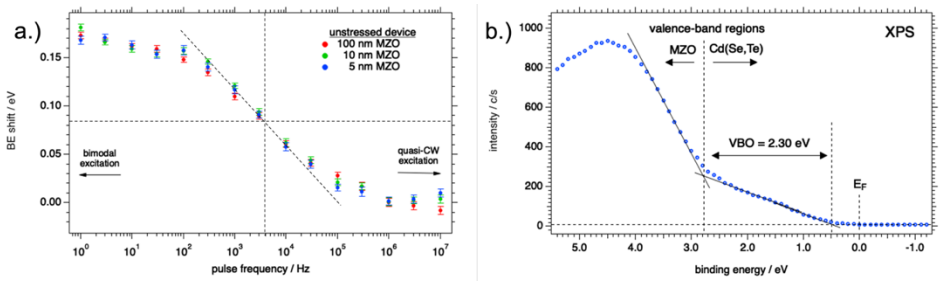

Figure 17. PopXPS measurements on the MZO/Cd(Se,Te) interface. Ar^+-ion etching was used to reduce the MZO thickness from its initial value (~100 nm) to less than the XPS information depth (~ 5 nm). (a) The popXPS characteristic transition frequency (4 kHz) was the same for all measurements, indicating that the interface properties were not substantially changed by the MZO etching process. (b) XPS valence-band measurement of the revealed 5-nm thick MZO/Cd(Se,Te) interface, from which the MZO-Cd(Se,Te) valence-band offset (VBO) is directly extracted.

After revealing the buried MZO/Cd(Se,Te), a popXPS experiment was performed to probe effects of in situ heat stress on the interface. In this experiment, summarized in Figure 18, the MZO/Cd(Se,Te) sample was heated to 135 °C for ~95 min., while XPS measurements tracked the Zn $2p_{3/2}$ and Cd $3d_{5/2}$ core-levels associated with the MZO and Cd(Se,Te) layers, respectively. Because these core-level binding energies precisely track the respective valence-band maximum (VBM) values of these layers, this provides a means for following changes in VBO during the in-situ stressing. During this experiment light bias was pulsed at 1 mHz to track photovoltage response. An unexpected result of this experiment, highlighted in Figure 18 (b), is that the measured VBO changes instantaneously with application of light bias condition, an effect that is observed throughout the experiment. To our knowledge, this phenomenon has not been previously reported in the literature, and we speculate that the cause of this effect is related to light-bias-induced changes in defect energy levels at the MZO/Cd(Se,Te) interface. Interestingly, the effect of light-bias on VBO increases at elevated temperature. The other significant finding is that the in-situ heating stress results in a permanent decrease in the VBO > 0.1 eV. This result is consistent with the KPFM results (cf. Figure 15) showing that in stressed devices a sharp peak appears in the electric field at the MZO/Cd(Se,Te) interface.

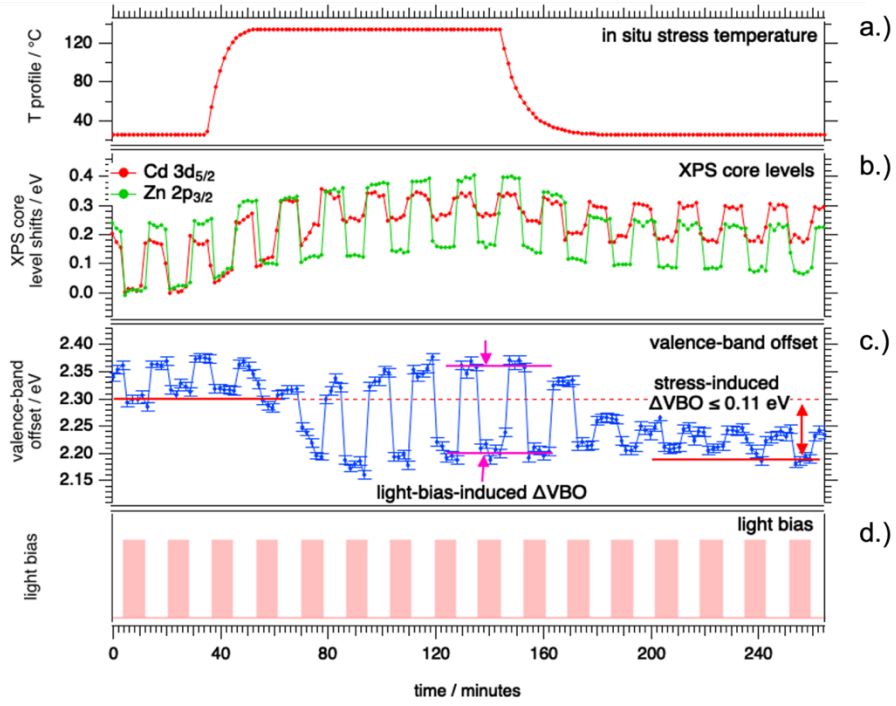

Figure 18. Summary of popXPS in situ stressing experiment on exposed MZO/Cd(Se,Te) interface showing: (a) temperature profile; (b) Cd $3d_{5/2}$ and Zn $2p_{3/2}$ core levels; (c) valence-band offset; and (d) light-bias profile.

EBIC measurements on stressed vs. unstressed Cd(Se,Te)/MZO devices:

Initial EBIC measurements were performed on standard CdTe- vs. Cd(Se,Te)-based

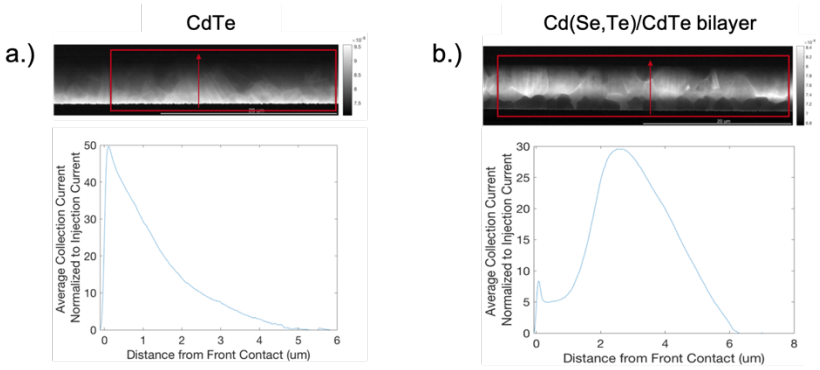

Figure 19. Comparison of standard EBIC profiles through the film thickness for a CdTe device (a) and a Cd(Se,Te)/CdTe bilayer device (b).

devices fabricated at NREL, which revealed collection behavior in the absorber that was previously unreported to our knowledge. As expected, the EBIC image from the CdTe devices in Figure 18 (a) is characterized by an exponential decay in current collection away from the junction. On the other hand, in the Cd(Se,Te) device [Figure 18 (b)] collection is peaked deep within the absorber. The position of this peak corresponds to the boundary between the alloyed Cd(Se,Te) layer (visible in the grain structure of the

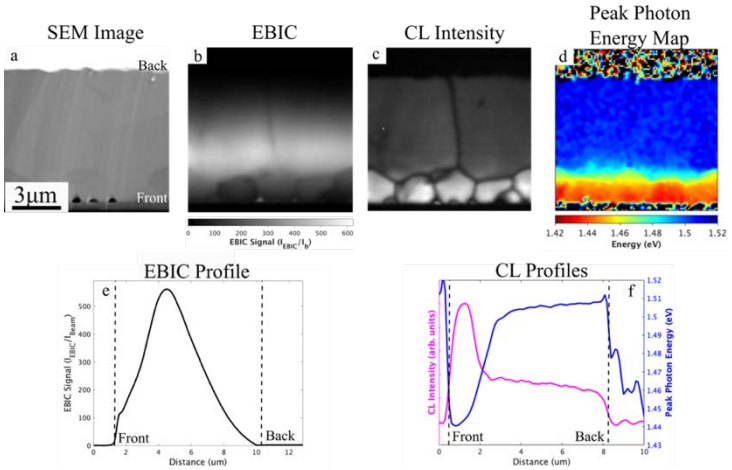

Figure 20. CL spectrum imaging and EBIC data acquired simultaneously on a Cd(Se,Te) absorber. (a) SEM image, (b) EBIC image, (c) CL integrated intensity image, and (d) peak photon energy map for the same location. (e) EBIC profile averaged over the image shown in (b). Front and back correspond to the bottom and top, respectively, of the EBIC image as shown in (a). (f) CL intensity and photon energy profiles averaged over the images in (c) and (d) EBIC image) and the pure CdTe region.

To further probe the unusual collection profiles observed in Cd(Se,Te) devices, experiments were performed that simultaneously acquired both EBIC and cathodoluminescence (CL) data sets under identical (short circuit) measurement conditions. In these measurements (summarized in Figure 20), complementary CL and EBIC profiles are observed. In other words, strong CL emission and weak EBIC collection are seen from the Cd(Se,Te) layer, and conversely, weak CL and strong EBIC signals are observed in the CdTe region and weak EBIC collection from the Cd(Se,Te) region. The CL photon energy map also reveals a markedly lower band gap within the alloyed Cd(Se,Te) region. These results further support the presence of a BHJ in absorbers composed of separately deposited and morphologically distinct Cd(Se,Te) and CdTe layers.

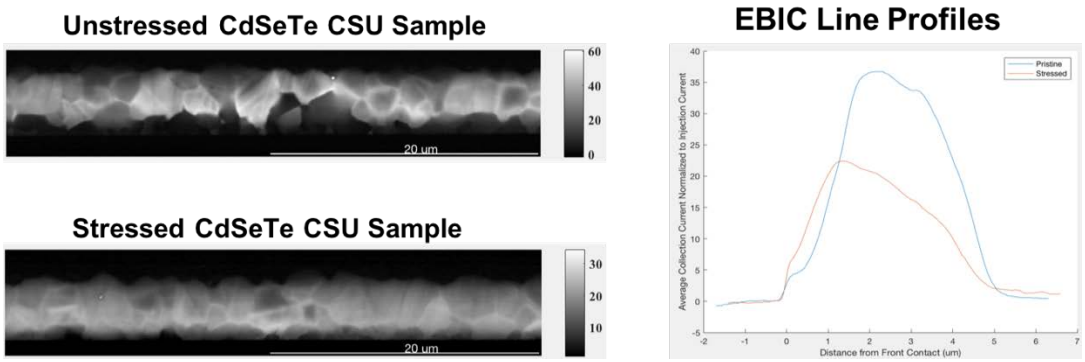

Figure 21. EBIC images of unstressed and stressed Cd(Se,Te) devices showing changes in the collection profile.

EBIC measurement were also performed on unstressed and stressed Cd(Se,Te) devices provided by CSU. These devices demonstrated unusual collection profiles very similar to those described above in studies on NREL devices, where instead of showing maximum collection near the front contact, CSU samples showed peak collection in the middle of the absorber layer. The EBIC images in Figure 21 illustrate changes in the collection behavior in the stressed devices. Whereas in the unstressed device there is strong contrast between the Cd(Se,Te) and CdTe regions, the stressed sample shows much lower contrast, and overall collection is higher in the Cd(Se,Te) layer.

TI measurements on stressed vs. unstressed Cd(Se,Te)/MZO devices:

TI measurements were performed to characterize diffusion length (L_d) values at different depths on stressed and unstressed Cd(Se,Te)/MZO devices. For the TI study, the stress conditions were 100 ºC at 0.8 sun for 15.75 h. During stressing, V_{oc}, FF, and efficiency dropped by 5.02, 36.8, and 38.0%, respectively. J_{sc}, on the other hand, increased by 3.2%. The previously described dimpler polishing technique expanded the analysis area by >100 times in a 5-μm-thick device, making it possible for TI to scan any area of interest across the device. Areas at different depths (close to the MZO, in the middle of the absorber, and near the back contact) were characterized by EBSD, near-field cathodoluminescence (NF-CL), and TI. EBSD mapping served as verification of surface crystalline quality and revealed relative grain size distributions in the bevel samples. As was observed in standard CL measurements (cf. Figure 20) NF-CL results showed the highest luminescence intensity in the Cd(Se,Te).

Figure 22 shows representative TI images at various depths of the two stressed and unstressed devices. No clear trend was identified for L_d between unstressed and stressed devices, indicating that the observed performance changes after stress are not related to a deterioration of the material properties that control diffusion length.

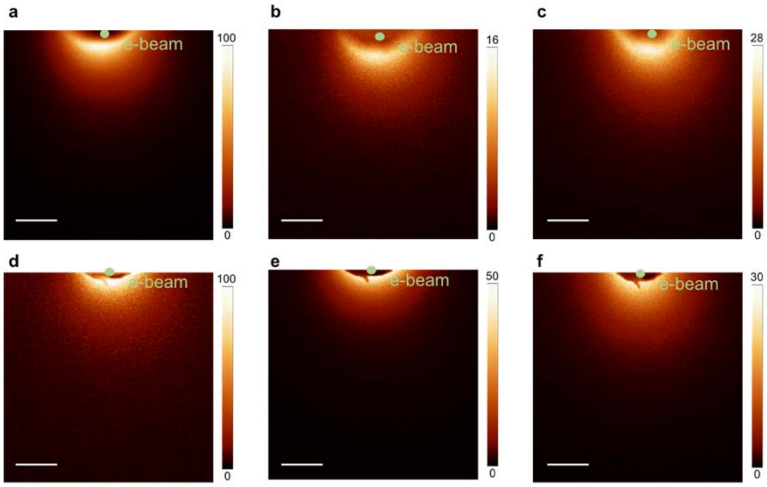

Figure 22. TI-based carrier-transport mapping: (a) unstressed device, near the MZO interface; (b) unstressed device, in the center of the absorber; (c) unstressed device, near the back contact; (d) stressed device, near the MZO interface; (e) stressed device, in the center of the absorber; (f) stressed device, near the back contact. The scale bars are 3 μm.

Subtasks 2.3.2 and 2.3.3 are both related to modeling Cd(Se,Te)/MZO devices; and **Subtask 3.3.1** summarizes the integration of characterization and modeling tasks to understand degradation in stressed devices.

7.3.3 Subtask 2.3.2: Demonstrated less than 20% deviation between simulated device parameters (V_{OC}, J_{SC}, FF, PCE) and actual measured performance of baseline (unstressed) Cd(Se,Te)/MZO devices, using model input parameters derived from correlative TI, CL/EBIC, TRPL, popXPS, KPFM and sMIM measurements.

7.3.4 Subtask 2.3.3: Demonstrated less than 20% deviation between simulated device parameters (V_{OC}, J_{SC}, FF, PCE) and actual measured performance of stressed baseline Cd(Se,Te)/MZO devices, using model input parameters derived from correlative TI, CL/EBIC, TRPL, popXPS, KPFM and sMIM measurements.

7.3.5 Subtask 3.3.1: Identified degradation mechanism(s) responsible for changes in next-generation CdTe devices using group-V dopants, Cd(Se,Te), and MZO films based on findings from 2.3.1, 2.3.2, 2.3.3.

Models were developed during this project to identify causes of degradation during heat/light stress. Device properties before and after stress were determined by comparing simulation results to data from several characterization techniques. Table III provides a summary of key parameter values and their sources. Cd(Se,Te)/MZO device

models were developed with p/n heterojunction and buried homojunction (BHJ) configurations. The BHJ model was based on electric potential profiles determined from KPFM data sets. Degradation mechanisms tested in the models included an increase in MZO/Cd(Se,Te) interface defects, variations of conduction band offsets at the MZO/Cd(Se,Te) interface, and MZO doping loss during light/heat stress. Comparison of device simulations to JV data [Figure 23 (a)] indicate that both the p/n heterojunction and BHJ models can account for the pre-stress and post-stress measurements. Both models exhibit the characteristic FF loss and flattening of the JV curve near V_{oc}. However, the BHJ model can better describe the electric field distribution changes observed by KPFM [Figure 23 (b)]. The observed increase in electric field at the back contact suggests a lowering of the work function there (i.e., increase in back barrier height), which is also clear in Figure 23 (b). A decrease in the MZO affinity of 0.1 eV was also observed in the XPS data, resulting in an increased spike conduction band offset at the Cd(Se,Te)/MZO interface.

Overall, the integrated set of results indicate that the performance degradation shown in Figure 23 (a) was caused by an decrease in MZO n-type doping and/or an increase MZO/Cd(Se,Te) acceptor-type interface defect density, along with an increase in the MZO/Cd(Se,Te) conduction band offset (see Table III for values) [15].

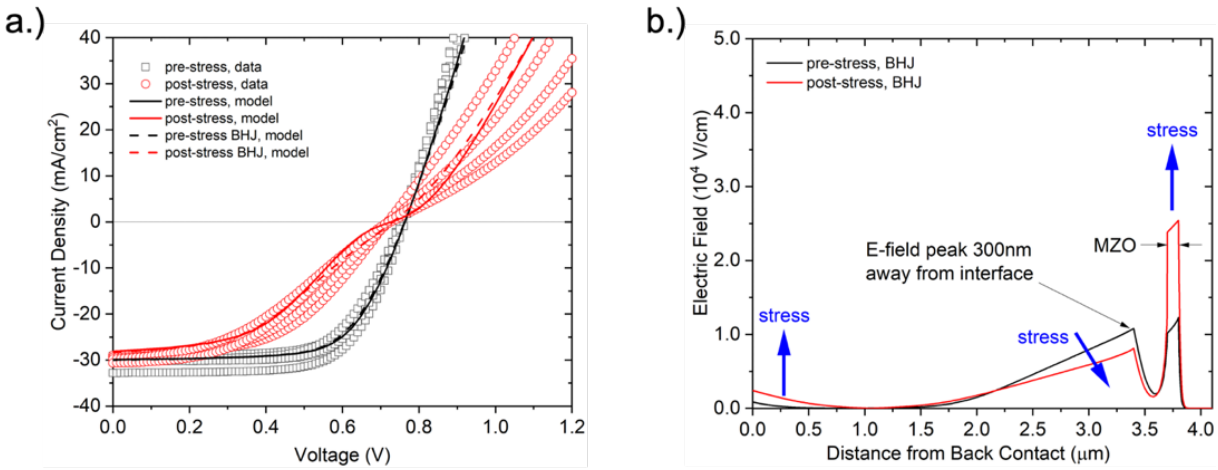

Figure 23. (a) JV curves for Cd(Se,Te)/MZO devices before (squares) and after (circles) light/heat stress. Pre- and post-stress simulation results are shown for the heterojunction model (solid lines) and BHJ model (dashed lines). (b) calculated electric field profiles from the BHJ model before and after stress.

Table III. Parameter values and source data for pre- and post-stress models.

Parameter	Unit	Pre-stress	Post-stress	Data	Observations, effects of heat/light stress
Junction Type		Buried HJ	Buried HJ	KPFM	• buried E-field peak in pre-stress Cd(Se,Te) devices
MZO affinity	eV	4.3	4.2	XPS	• FF loss due to CBO increase after stress
Cd(Se,Te)/MZO interface defect density	cm^{-2}	$< 10^9$	10^9 - $5x10^{10}$	JV, KPFM, XPS	• JV roll-under and FF loss due to lower E-field in Cd(Se,Te) • increased field at Cd(Se,Te)/MZO interface or in MZO • reduction in VBO after stress
MZO doping	cm^{-3}	$10^{14} – 10^{17}$	$10^{14} – 10^{16}$		• assumed low constant value but may start high and decrease with stress
CST carrier lifetime	ns	2	1.25	JV, CL	• slight V_{oc} and FF losses after stress
CST doping	cm^{-3}	4×10^{14}	3×10^{14}	CV	• increase in depletion width after stress
Back contact work function	eV	5.6	5.5	KPFM	• increase in E-field near back contact after stress
Series resistance	Ω cm^2	2.5	3.5	JV	• increase in resistance for $V > V_{oc}$ after stress
Band gap smoothing	μm	0.8	2.4	TI, EDS	• diffusion of Se with stress decreases band gap gradient.

7.4 Task 4: Application to Hybrid-Perovskite Solar-Cell Degradation Mechanisms.

This task applied novel characterization techniques, including in situ stressing and operando approaches, to understand degradation modes in hybrid perovskite/LiF/C60 devices (Figure 24) and identify dominant degradation mechanisms.

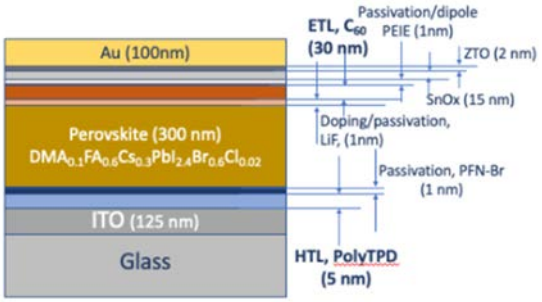

Figure 24. Schematic of the perovskite solar cells studied in this project (supplied through an NREL/industry partnership).

7.4.1 Subtask 2.4.1: Documented cell-level degradation modes in baseline perovskite/C60/SnO_x/Al devices with initial performance in the 15-18% efficiency range that track changes in device parameters (V_{OC}, J_{SC}, FF, PCE) vs. time.

Performance degradation of hybrid perovskite solar cells, provided through an NREL/industry partnership, was documented using NREL's SPA (solar parameter analysis) system. In these experiments, samples were held near maximum power point under 1-sun illumination for 1000 hours at 50 °C under N_2 atmosphere. The SPA data set [Figure 25 (a)] shows that photovoltaic conversion efficiency (PCE) dropped from an initial average value above 17% to ~12.5%. The majority of performance loss documented by the SPA testing was associated with decreases in J_{SC} and FF, whereas V_{OC} values remained relatively constant. Performance of these devices was also documented using a standard solar simulator before and after the SPA degradation testing as shown in Figure 25 (b). For reasons that were never adequately understood, the before and after JV measurements showed markedly different behavior of the solar cell degradation, most notably that the major loss in performance was associated with a loss in V_{OC} by more than a factor of 2. Unfortunately, these stress testing results came toward the end of the project period of performance, and due to other priorities the NREL perovskite core project could not devote additional SPA testing band width to repeat the experiments.

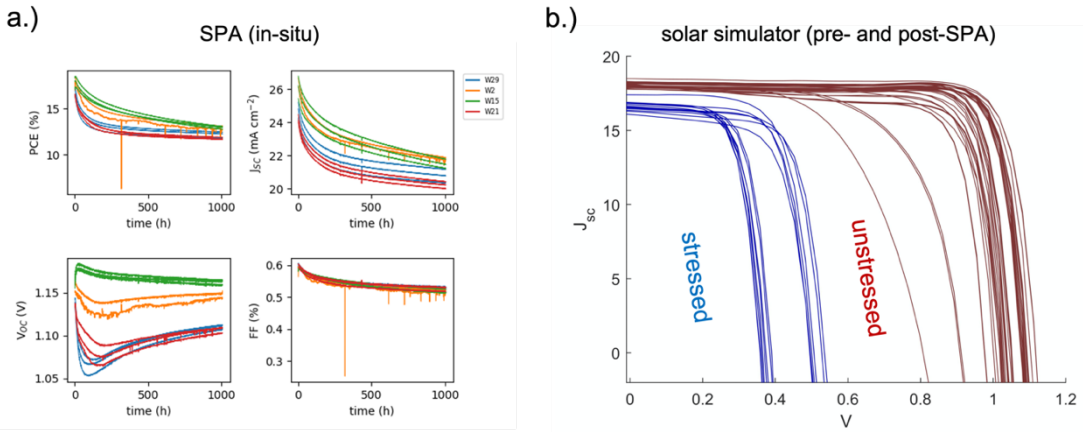

Figure 25. Comparison of a.) in situ SPA degradation tests and b.) pre- and post-SPA solar simulator measurements on hybrid perovskite solar cells.

7.4.2 Characterization of Unstressed and Stressed Cd(Se,Te)/MZO Devices

KPFM Measurements on Hybrid Perovskite Solar Cells:

Hybrid perovskite devices with the structure illustrated in Figure 24 were examined before and after stress testing with KPFM electric field profiling. These measurements showed that stressing primarily altered the electric field profile on the electron transport layer (ETL) side of the device. More specifically, after stressing a second peak

appeared in the electric field profile near the ETL/hybrid perovskite interface COMSOL device modeling showed that these results are consistent with a degradation mechanism in which the defect density at this interface increases from $8x10^{10}$ cm^{-2} to $1x10^{12}$ cm^{-2}.

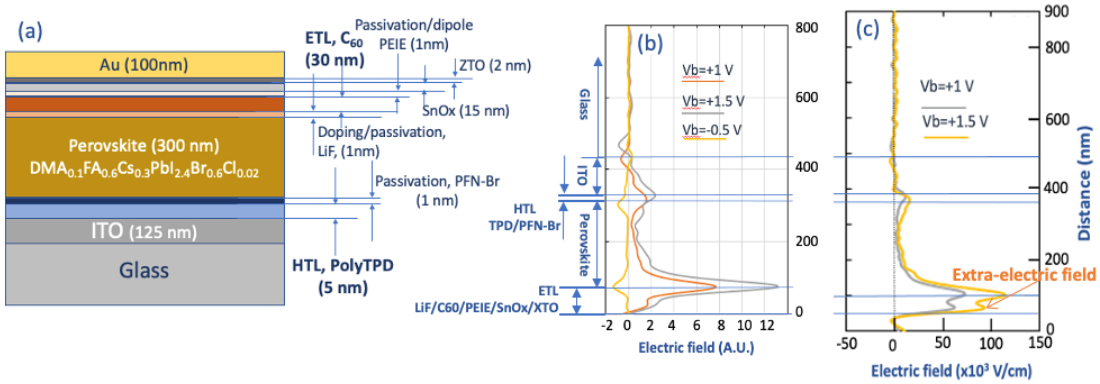

Figure 26. A schematic of the perovskite PV device, (b) and (c) electric field profiles taken on cross-sections of the unstressed and stressed devices under various applied voltage biases.

The KPFM potential profiling results for the unstressed device [Figure 26 (b)] show the electric field profile across the entire HTL/hybrid perovskite/ETL device stack, with peaks at both interfaces. The peak at the ETL interface is substantially stronger than at the HTL interface. This field distribution highlights the existence of uneven potential barriers, and possibly junction qualities, of the associated ETL and HTL interfaces. With the extensive stressing of 1000 h, a second electric field at the ETL side was found in addition to the original field at the interface [Figure 26 (c)], whereas the electric field in other regions of the device did not change significantly. This anomalous electric field indicates the degradation at the ETL side, and the observed V_{OC} loss is likely the result of photocarrier transport across the defective interface. Device modeling using COMSOL, in alignment with both JV and the KPFM electric field profile measurements, indicates that an increase in defect density at the C60/hybrid perovskite interface can significantly increase the electric field in the ETL layer and further cause an electric field spike at the SnO_x side of the ETL layer.

Optical TI Measurements on Hybrid Perovskite Solar Cells:

Regular TI is not suitable for perovskite work, because the electron-probe beam damages the surface of the samples during analysis. To eliminate this problem, a new optically excited TI (O-TI) system that uses a laser to excite the material was acquired. Although installation was delayed because of the pandemic, the system was successfully installed and tested during FY21.

The O-TI system was tested with GaAs and CdTe samples and showed very good results. Perovskite samples were aged with different degrees and analyzed in the new O-TI system. No deterioration was observed in perovskite samples during the analysis, in contrast to the rapid deterioration previously observed in similar samples analyzed in the conventional TI system. Figure 27 shows the analysis of the perovskite films. The results showed a decrease in diffusion length values that was correlated with a deterioration of the perovskite film stored at different conditions.

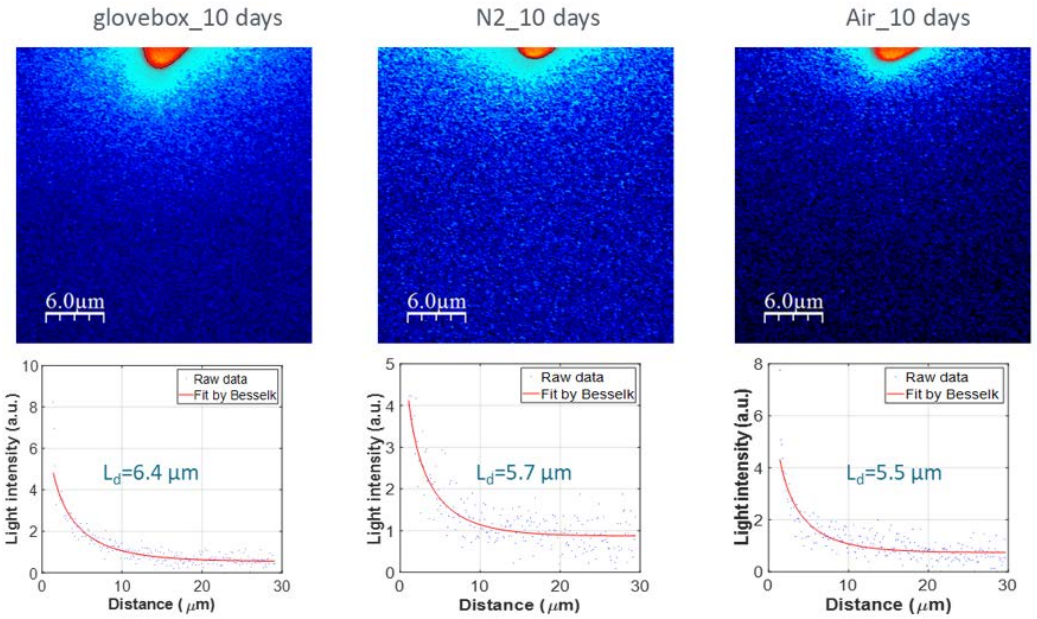

Figure 27. Optical TI maps (top) and diffusion length calculation for perovskite films stored at different conditions.

popXPS and popUPS Measurements on Hybrid Perovskites:

Initial popXPS measurements performed on unstressed hybrid perovskite devices (Figure 24) revealed that x-ray beam damage caused rapid deterioration in the photovoltage response. This effect is shown in the blue trace in Figure 28 (a). In this experiment, ~0.1 sun light bias was pulsed on and off with a period of 20 s while the Sn $3d_{5/2}$ core level (from a region on the device with exposed SnO_x) was monitored continuously. The pulsed light bias caused a photovoltage response on the order of 0.15 eV, which added to the initial ~0.9 eV shift associated with V_{OC} due to the x-ray excitation and stray light within the XPS vacuum chamber. This background V_{OC} decreased by a factor of 2 within ~ 7 minutes of x-ray exposure. Since a popXPS measurement series typically requires 60 minutes or longer to acquire, this observed degradation rules out meaningful popXPS measurements on hybrid perovskite devices.

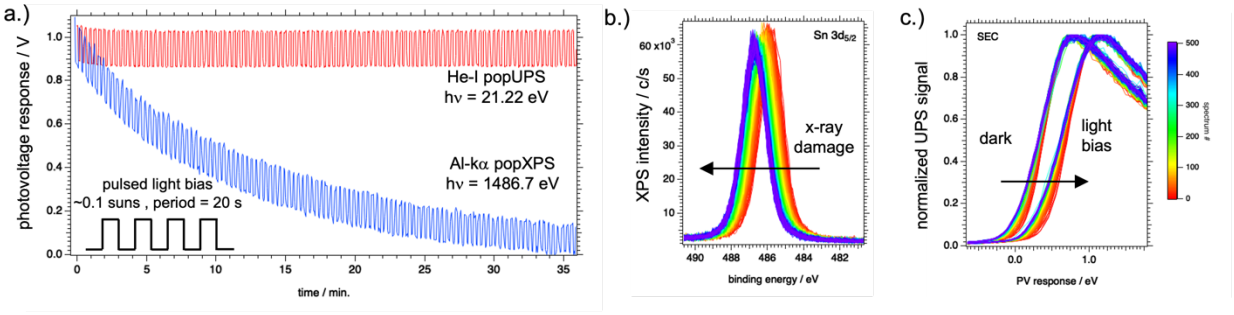

Figure 28. (a) Comparison of photovoltage response measured during popXPS vs. popUPS measurements on an unstressed hybrid perovskite solar cell. (b) Sn $3d_{5/2}$ core level during popXPS, showing an irreversible shift to higher binding energy associated with x-ray beam damage. (c) Secondary electron cutoff (SEC) spectra measured during popUPS.

In order to eliminate the issue of x-ray degradation, we developed a related technique that uses He-I ultraviolet (UV) excitation (hν = 21.22 eV) to monitor the secondary electron cutoff (SEC), as opposed to Al-ka radiation (hν = 1487 eV) to track core levels. The excitation depth of He-I UV photons is very shallow, likely ~1 nm or less, so the opportunity for optically induced degradation of perovskite materials is much less than for x-ray excitation. PopUPS measurements on the same hybrid perovskite device sample [red trace in Figure 28 (a)] show that the photovoltage response is very stable for the full duration of the experiment. The corresponding SEC regions are shown in Figure 28 (c).

Figure 29 compares popXPS measurements on a Cd(Se,Te)/MZO to popUPS measurements on a hybrid perovskite device. In both cases the pulsed light bias frequency was varied over the range 1 Hz to 10 MHz. In addition to completely mitigating the effects of x-ray damage on hybrid perovskite materials, another noteworthy benefit of the popUPS approach is that signal levels in UPS are substantially higher than for XPS. Consequently, the popUPS experiment can be performed more quickly (~ 20 minutes), with a higher density of sampled pulsed frequencies, and with significantly lower error bars, as can be seen in Figure 29.

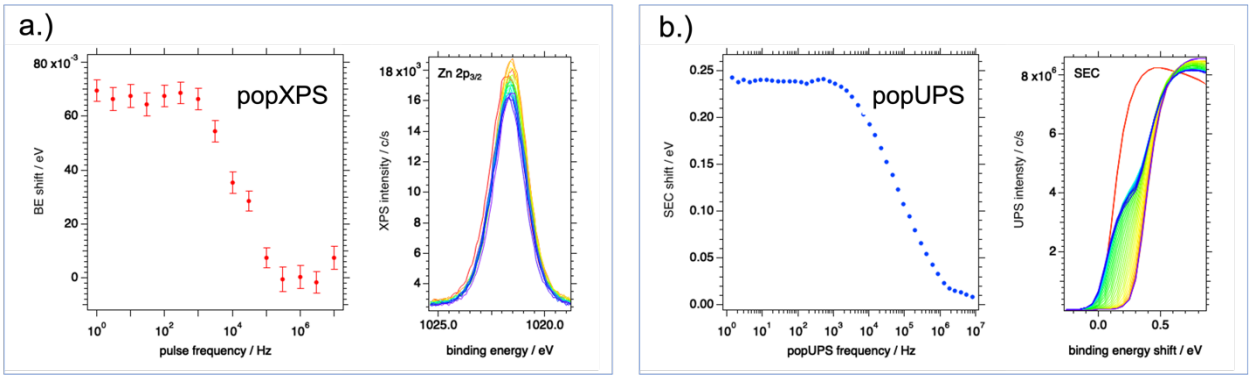

Figure 29. Comparison of (a) popXPS measurements on a Cd(Se,Te)/MZO with (b) popUPS measurements on a hybrid perovskite solar cell. The popUPS approach was developed to mitigate x-ray damage effects observed in perovskite materials.

In June through September 2021, the XPS instrument used to develop the popXPS and popUPS techniques was decommissioned and replaced with a state-of-the-art Physical Electronics Phi VersaProbe III instrument. The light sources and related electronics were successfully integrated onto the new instrument during Q1 of FY22. A final round of popXPS/popUPS measurements were planned on the unstressed and stressed Cd(Se,Te) and hybrid perovskite devices during FY22 Q2 and Q3. Unfortunately, the pulsed laser diode used in these experiments failed early in Q2. The laser was sent out for repair, but it was not returned in time to complete additional measurements prior to the end of the project period of performance.

sMIM Measurements on Hybrid Perovskites:

sMIM measurements were performed to evaluate the dependence of spectral and spatio-temporal properties of hybrid perovskite thin films on processing conditions and degradation under ambient exposure. Shown in Figure 30 (a)-(d) are the AFM

topography and MIM photoconductivity images of a MC hybrid perovskite thin film with time from ambient exposure indicated. These spatial photoconductivity maps reveal that degradation results in locally reduced regions of photoconductivity that correlate with topographic grain-like features. Examining the time domain traces [Figure 30 (e)] and action spectra [Figure 30 (f)] acquired over the evolution of the degradation reveals that although the carrier lifetimes are not significantly altered, a clear redshift of the absorption edge is seen. This suggests that although the local trap density is not changing significantly, the absorption redshift likely arises from halide segregation resulting in low-bandgap iodine rich regions. Importantly, we emphasize that no spatial variations in carrier lifetime and absorption onset is seen, which we interpret to be the result of the formation of iodine- and bromine-rich regions with characteristic length scales smaller than the ~50 nm achieved by our technique.

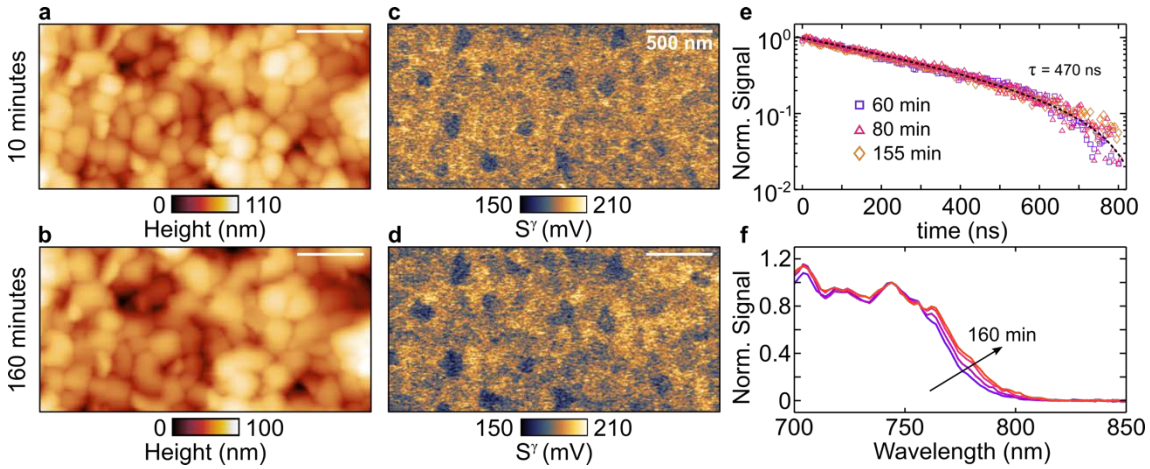

Figure 30. Spatially resolved AFM and photoconductive MIM imaging (a-d) of a MC perovskite film with exposure time to ambient conditions and illumination indicated. Evolution of time-domain (e) and spectral (f) characteristics under degradation.

For the FACs films (not shown) we find that increasing the processing annealing temperature from 100 ˚C to 180 ˚C results in regions of locally decreased photoconductivity that often correlates with morphologically apparent grain-like regions. These regions do not appear to result in local changes in the spectral characteristics or carrier lifetime, but likely due to a local impediment to carrier diffusion. Unlike the MC formulations, the primary degradation pathway of FACs formulations is transitioning to the “yellow” phase.

Subtasks 3.4.1 and **3.4.2** are both related to modeling hybrid perovskite devices, and **Subtask 3.3.1** summarizes the integration of characterization and modeling tasks to understand degradation in stressed devices.

7.4.3 Subtask 3.4.1: Demonstrated less than 20% deviation between simulated device parameters (V_{OC}, J_{SC}, FF, PCE) and actual measured performance of baseline (unstressed) hybrid perovskite/C60/SnO_x/Al devices, using model

input parameters derived from correlative TRPL, popXPS, KPFM and sMIM measurements.

7.4.4 Subtask 3.4.2: Demonstrated less than 20% deviation between simulated device parameters (V_{OC}, J_{SC}, FF, PCE) and actual measured performance of stressed baseline hybrid perovskite/C60/SnO_x/Al devices, using model input parameters derived from correlative TRPL, popXPS, KPFM and sMIM measurements.

7.4.5 Subtask 3.4.3: Publication identifying degradation mechanism(s) based on findings from 4.1, 4.2, 4.3, specifically, addressing whether interfacial degradation is still a limiting factor, or if degradation of the bulk absorber now dominates.

Hybrid perovskite device models were based on the architecture described in Figure 24 and information provided in the literature.[11],[19]-[25] Baseline model JV curves along with several measurements are provided in Figure 31 (a). Model parameters are provided in Table IV. The baseline model compares well with the higher performing cells in the group (efficiency > 16%). The JV curves after heat/light stress shown in Figure 31 (b) indicate a significant loss of Voc after stress. KPFM electric potential profiles suggested charge-related variations at the ETL/hybrid perovskite interface with stress. We therefore considered a parameter space with the electron affinity of the ETL layer (χ_{C60}) and the interface defect density $N_{i(per/C60)}$. An increase in χ_{C60} to 4.5 eV (conduction band cliff) and $N_{i(per/C60)}$ to 10^{12} cm^{-2} can account for the observed degradation, as indicated by the blue solid line in Figure 31 (b). Those parameters also result in an increase in the ETL electric field and corresponding decrease in the hybrid perovskite, as observed by KPFM. These results suggest that defects and related band off-sets at the C60/hybrid perovskite interface (LiF layer) are the primary source of degradation.

Table IV. Hybrid perovskite baseline device model parameters.

Parameter	Symbol	Unit	Hybrid perovskite	polyTPD	C60	SnOx
band gap	E_g	eV	1.73	3.0	1.73	3.6
elec. affinity	χ	eV	4.0	2.4	4.12	4.2
rel. permittivity	ε_r		6.5	3.0	4.25	9
mobility (e/h)	μ_n/μ_p	cm^2/Vs	2/2	$2x10^{-4}/2x10^{-4}$	1.6/1.6	240/25
lifetime (e/h)	τ_n/τ_p	ns	192/192	5/5	1/1	100/100
doping (p/n)	N_A/N_D	cm^{-3}	n: 10^9	p: 10^{18}	n: 10^{12}	n: 10^{17}
DOS cond. band	N_C	cm^{-3}	$2.2x10^{18}$	$2.2x10^{18}$	$2.2x10^{18}$	$4.4x10^{18}$
DOS val. band	N_V	cm^{-3}	$1.8x10^{19}$	$1.8x10^{19}$	$1.8x10^{19}$	$2.5x10^{19}$

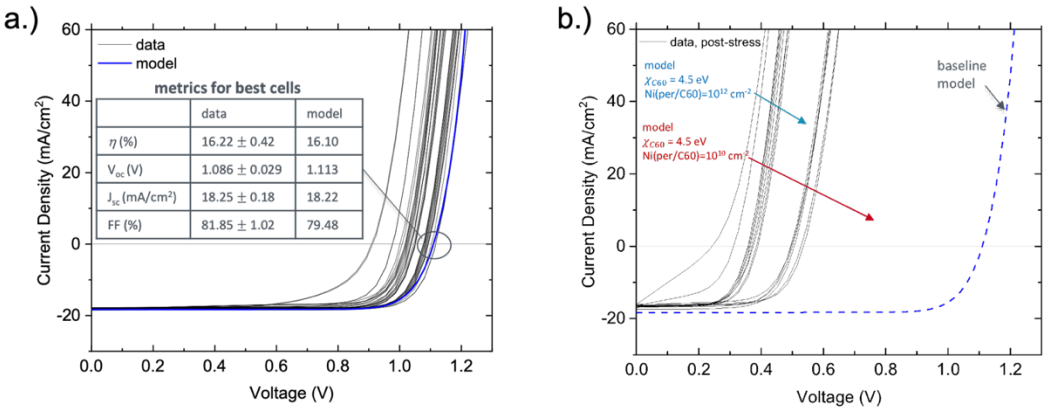

Figure 31. (a) hybrid perovskite device JV curves before heat/light stress for several measurements (black curves) and the model (blue). (b) post-stress JV curves with measured values (black) and two model cases. Dashed curve is the pre-stress, baseline model.

7.5 Task 5: Correlative EO and Chemical Analysis for Buried Perovskite Interfaces

In year 1 of the project, we analyzed interface and bulk recombination in narrow bandgap (E_g=1.25 eV) Sn/Pb hybrid perovskites. This data is illustrated in Figure 32, where (A) shows fluence-dependent TRPL data and indicates very low impurity level in these materials (estimated from this data 1×10^{14} cm^{-3}).[26] Graph (B) shows absorber thickness dependent TRPL, and increased lifetime for thicker absorbers indicates reduced impact of interface recombination. Quantitatively, lifetimes from (B) are analyzed in (C), where we determine bulk carrier lifetime τ_b ~9.2 μs and interface recombination velocity S ~1.4 cm/s, both record values for low-E_g hybrid perovskites. Graph (D) shows temperature dependent TRPL lifetimes and analysis of this data to determine contributions from radiative recombination, defect-mediated recombination, and carrier trapping. As shown in (D), defect-mediated recombination is the most significant, and it further increases at device interfaces (Figure 33).[26]

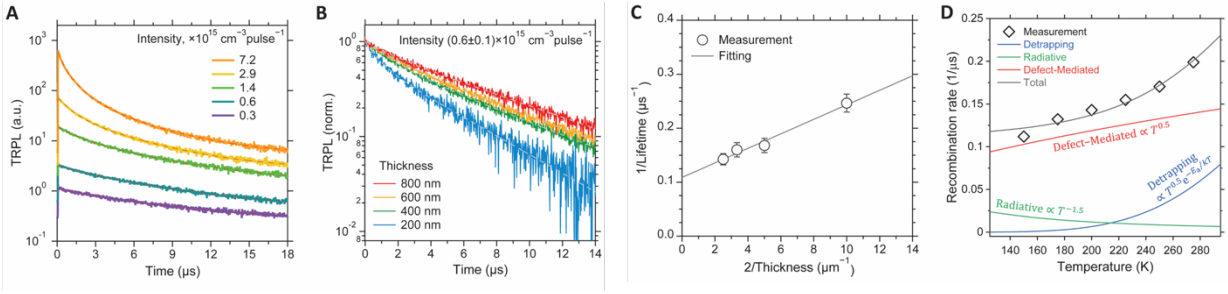

Figure 32. (A) Time-resolved photoluminescence (TRPL) measurement on ~800-nm-thick narrow-bandgap hybrid perovskite film prepared with the PEAI-GASCN additives under different excitation intensities (injection levels). (B) TRPL measurements of hybrid perovskite films with thickness varying from 200 to 800 nm. (C) Thickness dependence of the TRPL lifetime with analysis to extract the bulk carrier lifetime and the surface recombination velocity. (D) Temperature dependence of recombination rate (or lifetime^{-1}) from TRPL measurement. *T* is the temperature, E_a is the activation energy associated with shallow traps, and *k* is Boltzmann's constant. The laser excitation wavelength was 640 nm.

To develop analysis in Figure 32, we considered a range of characterization methods. This included using one-photon and two-photon excitation, varying excitation wavelength between 400 nm to 650 nm, and numerical modeling of charge carrier drift and diffusion in semiconductor absorbers. After trying these different approaches, the most informative characterization techniques were those illustrated in Figure 32. Earlier, such analysis was mostly used for III-V PV, but not for thin film characterization. Very low recombination evident in the data leads to charge carrier diffusion length that exceeds absorber thickness tens of times. Because of very large diffusion length, analysis based on measurements and modeling of different carrier generation profiles is less sensitive, while changing the absorber thickness to vary relative rates of interface and bulk recombination allows clear separation of interface and bulk lifetimes.

Figure 33 shows measurements to determine interface recombination velocity at electron (C_{60}) and hole (PEDOT:PSS) transport interfaces in the same system.[26] In comparison to near absorber (PVK), additional recombination is evident at both interfaces, and recombination is much larger at the HTL interface. Observed reduction in lifetime indicates HTL interface recombination losses of about 75 mV, which is close to total recombination loses in this system. Data summarized in Figures 1-2 identifies and quantifies losses in low-E_g hybrid perovskite solar cells used in record-efficiency hybrid perovskite-hybrid perovskite tandems.[26]

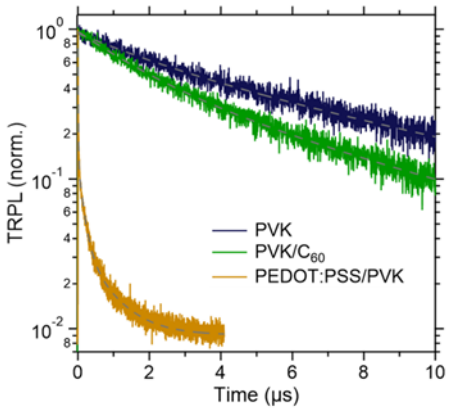

Figure 33. TRPL comparison of hybrid perovskite thin films prepared with PEAI and GASCN on glass without contact layers (noted as PVK), with C60 (noted as PVK/C60), and with PEDOT:PSS (noted as PEDOT:PSS/PVK). The average lifetimes are 8.4 μs (PVK), 5.2 μs (PVK/C60), and 0.47 μs (PEDOT:PSS/PVK).

In years 2 and 3, we also worked on voltage loss analysis in solar cells where the absorber is composed of hybrid perovskite quantum dots (PQDs, Figures 34-36).[27] Using PQDs enables all-inorganic large-E_g absorbers, currently not possible with spin-coated or evaporated hybrid perovskites. As identified in our studies, interfaces between PQDs in the absorber layer led to both positive and detrimental effects. First, we identified large carrier concentration (unintentional doping) in such films, up to 10^{17} cm^{-3}, which were attributed to interface defects.[27] Such high carrier concentration lowers

the hole Fermi level and enables large quasi-Fermi level separation (qFLS, also called implied voltage), even when carrier lifetimes are only in the 10 ns range. Because bulk lifetimes are in the 10 ns range, ETL and HTL interface quality is less important in such hybrid perovskites, and only PQD interfaces need to be optimized. Second, minority carrier traps were identified and quantified at PQD interfaces [Figure 34 (b) and (c)]. As also shown in Figure 34, such traps are associated with the A-site of the hybrid perovskite, and trap density is reduced for $FAPbI_3$ absorbers (this follows from the lower excitation fluence needed to saturate traps for $FAPbI_3$).

One of the challenges for characterizing recombination and voltage losses in PQD hybrid perovskites was relative complexity of this system, where we had to estimate background carrier density, trap density and energy, and carrier lifetime. The kinetic scheme we had to consider is given Figure 35. We solved this problem by using two modeling approaches. First, we modeled only low injection data, where it was possible to estimate trap density and energy. This analysis is based on carrier capture and release modeling. Second, with trap parameters fixed, we used a full kinetic model described in Figure 35 to determine background carrier density (doping) and minority carrier lifetime. By numerically solving this model for the full range of injection conditions, we were able to estimate doping and lifetimes for $CsPbI_3$, (Cs,FA)PbI_3, and $FAPbI_3$ PQDs, developing an understanding of origin of high voltage in hybrid perovskite quantum dot photovoltaics.[27]

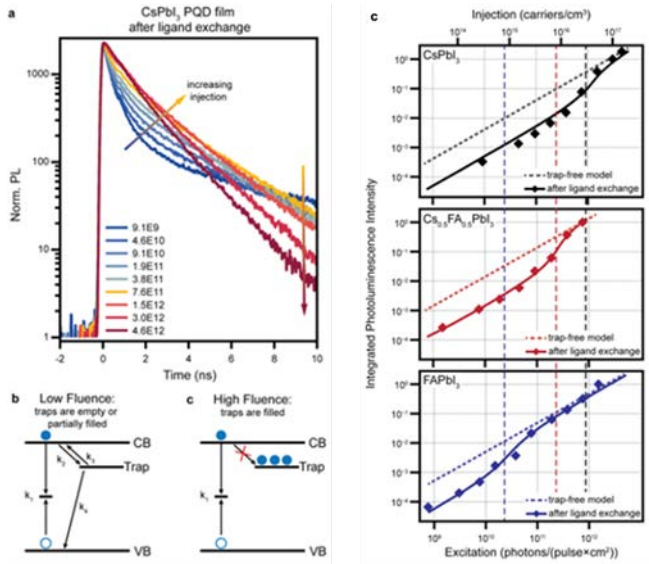

Figure 34. (a) Normalized TRPL data for $CsPbI_3$ PQD films after ligand exchange with varying 470 nm excitation photon fluence (photons/(pulse·cm^2)) indicated in the legend. Schematic indicating carrier dynamics at (b) low fluence and (c) high fluence. Right: Integrated photoluminescence (data points) *versus* excitation fluence with model results (lines) for $CsPbI_3$ (black), $Cs_{0.5}FA_{0.5}PbI_3$ (red), and $FAPbI_3$ (blue) PQD films. The trap density derived from the model results are plotted as vertical dashed lines.

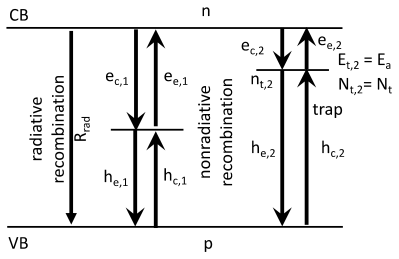

$$\frac{\partial n}{\partial t} = k_B T \mu \frac{\partial^2 n}{\partial z^2} + \sum_{i=1}^{2}\left(e_{e,i} - e_{c,i}\right) - R_{rad} + G \quad (1)$$

$$\frac{\partial p}{\partial t} = k_B T \mu \frac{\partial^2 n}{\partial z^2} + \sum_{i=1}^{2}\left(h_{e,i} - h_{c,i}\right) - R_{rad} + G \quad (2)$$

$$e_{e,i} = n_{t,i}\sigma_{n,i}v_{th}N_C exp\left(-\frac{E_{t,i}}{k_B T}\right) \quad (3)$$

$$e_{c,i} = n(N_{t,i} - n_{t,i})\sigma_{n,i}v_{th} \quad (4)$$

$$h_{e,i} = (N_{t,i} - n_{t,i})\sigma_{p,i}v_{th}N_V exp\left(-\frac{E_g - E_{t,i}}{k_B T}\right) \quad (5)$$

$$h_{c,i} = p n_{t,i}\sigma_{p,i}v_{th} \quad (6)$$

$$I_{PL}(t) = B\int_0^d \left(n(z,t)p(z,t) - n_i^2\right)dz \quad (7)$$

$$n_i = \sqrt{N_C N_V}\exp\left(-\frac{E_g}{2k_B T}\right) \quad (8)$$

Figure 35. Kinetic scheme used in PQD TRPL simulations and kinetic equations to describe recombination and trapping dynamics. Solving these equations for $I_{PL}(t)$ [eq. (7)] simulates injection-dependent TRPL data, some of which is shown in Figure 3.

To develop microscopic (micron-scale-resolution) EO voltage loss analysis, we again analyzed PQD hybrid perovskite devices. Device stack and geometry, measurement geometry, and data are illustrated in Figure 36. The objective was to map spatial qFLS (also called implied voltage) distribution, especially near device edges. Analysis is based on measuring microscopic map of minority carrier lifetimes and calculating minority carrier (electron) density n from such lifetime data. Using lifetime and carrier density data, we estimate qFLS(x,y) shown in Figure 36 (c) – (e) from

$$qFLS = E_g + \frac{k_B T}{e}\ln\left(\frac{np}{N_C N_V}\right) \quad (1)$$

Where k_B is Boltzmann's constant, T is temperature, e is elementary charge, N_C and N_V are densities of states. The qFLS histograms in (f) have maximum qFLS = 1.24 eV for a new device, but implied voltage is reduced to qFLS = 1.215 eV after 4 days in air. This voltage degradation increases as a distance from the device edge, suggesting buried interface degradation mechanism. Interface recombination velocity of about 4000 cm/s can be calculated from such data (shown in (g)), and the HTL interface recombination is largest where PTAA HTL is not protected from the ambient.

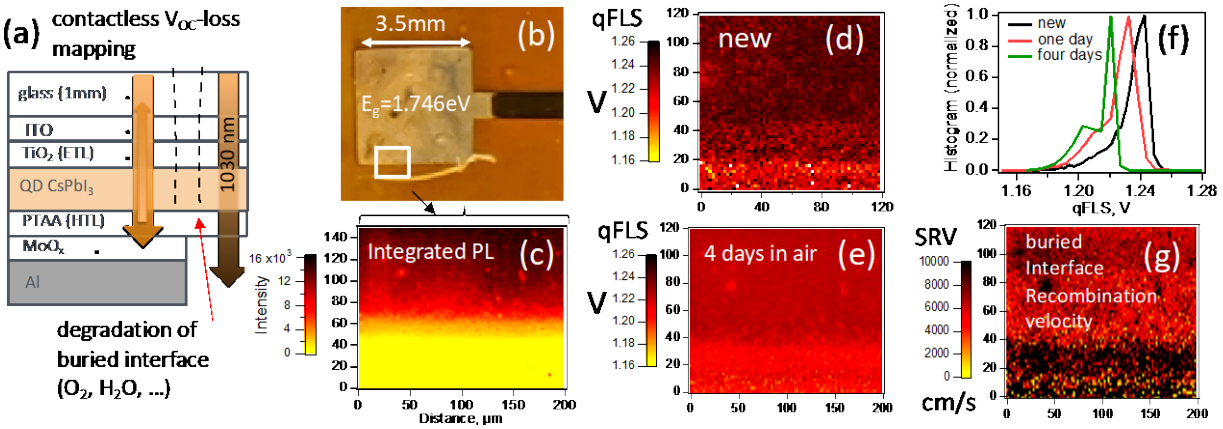

Figure 36. Recombination analysis from TRPL microscopy. (a,b): hybrid perovskite quantum dot device stack and measurement geometry, (c): PL intensity for area shown in b, (d,e): *qFLS* maps from Eq. (1a) for new solar cell and after degradation, (f) *qFLS* histograms for data in d, e, (g) map of buried HTL/(QD $CsPbI_3$) interface recombination velocity for data in (e). Figures (c), (d), (e), and (g) show approximately the same field of view/ the same device measured nondestructively though a 1-mm thick glass.

In addition to data summarized in Figures 32-36, we developed voltage loss characterization methods for all-back-contact (ABC) hybrid perovskite architecture. This data is shown in the year-3 quarterly review slides.

8 Significant Accomplishments and Conclusions

Task 1. PV Characterization Technique Development:

- Several approaches were developed for preparing cross-sectional and wedge samples with very low damage surfaces (as verified by EBSD measurements) suitable for subsequent electron- and scanning-probe-based measurements including TI, EBIC, and KPFM.
- A in situ stressing was built into the AFM-based nanoelectrical platform, the electrical signal noise level did not increase with the individual or combination of RT-85°C, 0-1 sun, and 0-1500 V stresses, and the sample drift was measured less than 15 mm/day.
- Novel methods, popXPS and popUPS, were developed for studying exposed PV interfaces. In this approach, XPS or UPS spectra are acquired while the sample is illuminated with pulsed light-bias. By acquiring spectra over a range of frequencies and using COMSOL device modeling to interpret spectral shifts and line shapes, popXPS/popUPS can reveal detailed information about carrier generation, migration, and recombination processes, and directly correlate these with critical interfacial properties including composition, chemical states, and energy-band alignments.

Task 2. Correlative Measurement and Device Model Development and Validation:

- COMSOL-based device-physics simulation capabilities were developed for e-beam characterization techniques, including TI, CL, and EBIC.

- Model analysis of TI results for Cd(Se,Te)/MZO devices demonstrated that the anomalous second peak observed in the data was caused by band gap grading in the Cd(Se,Te) layer. The second peak disappeared after stress due Se diffusion and the associated band gap smoothing
- Simulations of CL and EBIC for pre- and post-stress Cd(Se,Te)/MZO devices agree with data that carrier lifetime decreases slightly during heat/light stress and e-beam current collection decreases significantly.
- Pulsed-light popXPS simulations were developed and indicated that the observed binding energy shift was an observation of open circuit voltage decay, which can be used to determine carrier transport properties when combined with other characterization techniques.

Task 3. Application to CdTe Solar-Cell Degradation Mechanisms:

- TI, EBIC and CL measurements on Cd(Se,Te)/MZO devices revealed unusual complementary luminescence and collection profiles that changed significantly in stressed devices. Combined with device-modeling, these results indicated the existence of a buried homojunction in the Cd(Se,Te)/CdTe bilayer absorber whose characteristics degraded upon stressing.
- KPFM potential profiling across Cd(Se,Te) devices demonstrated directly a BHJ as the working junction and the second electric field at the heterointerface associated with device reversible metastability and irreversible degradation. Both the device degradation and the electric field at the heterointerface were caused by reduction of doping in the MZO buffer layer by the stressing.
- popXPS measurements on the exposed MZO/Cd(Se,Te) interface showed that in situ stressing at elevated temperatures resulted in a permanent change in valence-band offset. Additionally, the popXPS measurements showed that the interfacial band alignment in these devices changed with light bias, revealing the existence of charged interfacial defects with light-bias-dependent populations.
- The primary cause of Cd(Se,Te)/MZO device degradation was a decrease in donor-type MZO doping and/or an increase in acceptor-type Cd(Se,Te)/MZO interface defects, along with a decrease in the MZO electron affinity.

Task 4. Application to Hybrid-Perovskite Solar-Cell Degradation Mechanisms:

- An anomalous additional electric field at the ETL side of a degraded hybrid perovskite device was found by KPFM potential profiling. Both the V_{OC} loss and this electric field was caused by an increase in interface defect states.
- popXPS and related measurements on perovskite materials and devices revealed that x-ray-induced degradation on these materials causes very rapid (timescale of minutes) degradation of critical material properties, as revealed by loss in V_{OC}. If not properly accounted for this type of material degradation would lead to flawed measurements and conclusions. To mitigate the issue of x-ray degradation, the alternative technique popUPS was developed, which provides a means for assessing V_{OC} related phenomena in hybrid perovskite devices.
- The primary cause of hybrid perovskite device degradation was a decrease in the C60 electron affinity, causing a conduction band cliff at the interface with the

hybrid perovskite layer, and an increase in the C60/hybrid perovskite interface defect density.

Task 5. Correlative EO and Chemical Analysis for Buried Perovskite Interfaces:

Our goal in this task was to develop EO voltage loss analysis techniques and apply them to state-of-the art hybrid perovskite solar cells. In Section 7, we presented a summary of such analysis for two device architectures: 1) low-E_g absorbers with extremely long, ~10 us, charge carrier lifetime and low impurity density and 2) high-E_g PQD absorbers with high doping but relatively short minority carrier lifetimes. In the first case we separated bulk and interface recombination and identified dominant loses at HTL interface. In the second case we identified that losses predominantly occur at PQD interfaces in the absorber, not at device interfaces. A wide range of PL-based time-resolved measurements and modeling were used, and appropriate methods for low-doped and high-doped absorbers were identified and applied.

Our results contributed to developing record-efficiency hybrid perovskite tandems[Error! Bookmark not defined.] and to understanding origins of high voltage in quantum dot hybrid perovskite solar cells.[Error! Bookmark not defined.] Techniques developed in this project can be used in future hybrid perovskite research (including advanced architectures, such as buried interface characterization in tandems, etc.) and we are making efforts to continue this work. The most important remaining limitation for EO voltage loss analysis is need for faster measurements for metrology. For example, data in Figure 5 is collected at ~0.7 s /pixel. There are 2500 pixels in this data, and measurement time is ~40 min. We look forward to opportunities to use faster wide field imaging for EO property mapping and analysis.

9 Budget and Schedule

The total budget for the project (initially FY19-FY21) was $3.63M (federal share) with no cost share. Spending on the project slowed down and fell behind schedule by roughly one quarter ($100k) in FY20 due to the onset of pandemic. During FY21, a no-cost technical extension (NCTE) for the project was requested and granted by DOE for three additional quarters (FY22 Q1-Q3) to complete laboratory work, with an additional quarter (FY22 Q4) to complete reporting requirements. The project carried a substantial balance into FY22, the bulk of which was planned for completing popXPS/popUPS experiments and summarizing these results in journal paper. Unfortunately, equipment problems (a failed laser diode) prevented planned experiments from taking place in FY22 Q2-Q3, and consequently ~ 2.3% of the initial three-year budget ($83k out of $3.63M) was unspent as of the end of August 2022.

10 Path Forward

The EBIC and CL approaches developed within this project are continuing to be used in projects that include

- From Devices to Atoms: Assessing Perovskite Device Stability and Metastability by Spatially Resolved In-Situ and Targeted Ex-Situ Characterization DE-EE000 38044 - PI Dana Kern, NREL
- In-situ antimony doped polycrystalline CdTe films for simplified cell processing and maximized energy Award # DE-EE0009344 – PI Bill Shafarman, University of Delaware

The AFM-based approaches are being applied in projects including

- NREL CdTe core project: As-doped CdSeTe
- CSU's advanced CdSeTe device structures (with possible funding under the recently announced CdTe Accelerator Consortium (CTAC)s
- A proprietary project with a CRADA partner

The operando XPS based techniques have been used in

- an initial collaboration with a U.S.-based Si PV manufacturer
- an exploratory collaboration with the NREL Si PV Core Project

Electro-optical approaches developed under task 5 continue in the following projects:

- A new NREL project funded under LabCall 38525, with focus on voltage loss analysis in CdTe devices (recombination, band tails, contact selectivity); PI Darius Kuciauskas
- The new techniques that were developed for perovskite characterization have a small role in several NREL projects in FY22

11 Inventions, Patents, Publications, and Other Results

1. C. Xiao, C.-S. Jiang, K. Blaine, M. Amarasinghe, E. Colegrove, W. K. Metzger, M. M. Al-Jassim, N. M. Haegel, H. Moutinho, Direct microscopy imaging of nonuniform carrier transport in polycrystalline cadmium telluride, Cell Reports Physical Science, 1 (10), 2020, 100230, doi.org:10.1016/j.xcrp.2020.100230

2. Chuanxiao Xiao, Chun-Sheng Jiang, Marco Nardone, David Albin, Adam Danielson, Amit H. Munshi, Tushar Shimpi, Walajabad Sampath, Sean Jones, Mowafak M. Al-Jassim, Glenn Teeter, Nancy M. Haegel, and Helio R. Moutinho, Microscopy Visualization of Carrier Transport in CdSeTe/CdTe Solar Cells, ACS Appl. Mater. Interfaces, 14 (35), 2022, 39976, doi.org:10.1021/acsami.2c09426

3. M. Al-Jassim and N. Haegel, Eds., Advanced Characterization of Thin Film Solar Cells. Institution of Engineering and Technology, 2020. [Online]. Available: https://digital-library.theiet.org/content/books/po/pbpo166e

4. C.-S. Jiang, D. Albin, M. Nardone, K.J. Howard, A. Danielson, A. Munshi, T. Shimpi, C. Xiao, H.R. Moutinho, M.M. Al-Jassim, G. Teeter, W. Sampath, Electrical potential investigation of reversible metastability and irreversible degradation of CdTe solar cells, Sol. Energy Mater. Sol. Cells, 238, 2022, 111610, doi.org:10.1016/j.solmat.2022.111610

5. C.-S. Jiang, D. Albin, M. Nardone, K.J. Howard, A. Danielson, A. Munshi, T. Shimpi, W. Sampath, C. Xiao, H.R. Moutinho, M.M. Al-Jassim, G. Teeter, Metastability and Degradation of CdTe Solar Cells Investigated by nm-Scale Electrical Potential Imaging, presented at 49th IEEE PVSC, 2022

6. S. Berweger, F. Z., B.W. Larson, A.J. Ferguson, A.F. Palmstrom, O.G. Reid, T.M. Wallis, K. Zhu, J.J. Berry, P. Kabos, S.U. Nanayakkara, Nanoscale Photoexcited Carrier Dynamics in Perovskites, J. Phys. Chem. Lett. 2022, 13, 10, 2388–2395, doi.org:10.1021/acs.jpclett.2c00233

7. J. Tong, Q. Jiang, A. J. Ferguson, A. F. Palmstrom, F. Zhang, J. Hao, S. P. Dunfield, A. E. Louks, H. Lu, R. M. France, S. A. Johnson, M. Yang, J. F. Geisz, M. D. McGehee, M. C. Beard, D. Kuciauskas, J. J. Berry, and K. Zhu, Cation-engineered carrier control in efficient Sn-Pb narrow-bandgap hybrid perovskite tandem solar cells, Nat Energy **7**, 642–651 (2022). doi.org:10.1038/s41560-022-01046-1

8. B.M. Wieliczka, J.A. Márquez, A.M. Bothwell, Q. Zhao, T. Moot, K.T. VanSant, A.J. Ferguson, T. Unold, D. Kuciauskas, and J.M. Luther, Probing the Origin of the Open Circuit Voltage in Hybrid perovskite Quantum Dot Photovoltaics, ACS Nano 15, 2021, 19334, doi:10.1021/acsnano.1c05642

12 References

[1] J. Kettle *et al.*, Review of technology-specific degradation in c-Si, CdTe, CIGS, dye sensitized, organic and perovskite solar cells in photovoltaic modules: Understanding how reliability improvements in mature technologies can enhance emerging technologies, *Progress in Photovoltaics: Research and Applications*, 2022, doi: 10.1002/pip.3577.

[2] C.-A. Hsu, V. Palekis, S. Levcenko, D. Morel, and C. Ferekides, Cu-doping Effects in CdSexTe1-x/CdTe Solar Cells, 2019, pp. 1839–1842. doi: 10.1109/PVSC40753.2019.8980648.

[3] Y. Samoilenko *et al.*, "Stable magnesium zinc oxide by reactive Co-Sputtering for CdTe-based solar cells," *Solar Energy Materials and Solar Cells*, vol. 210, 2020, doi: 10.1016/j.solmat.2020.110521.

[4] J. Liu *et al.*, "Transmission Electron Microscopy Study on Microstructure of Degraded CdTe Mini-Modules," *IEEE Journal of Photovoltaics*, vol. 9, no. 3, pp. 893–897, 2019, doi: 10.1109/JPHOTOV.2019.2893854.

[5] A. Masuda, Y. Hara, Y. Shiina, S. Okamoto, and T. Okamoto, "Similarity of potential-induced degradation in superstrate-type thin-film CdTe and Si photovoltaic modules," *Japanese Journal of Applied Physics*, vol. 58, no. SB, 2019, doi: 10.7567/1347-4065/aafe67.

[6] M. K. Rao, D. N. Sangeetha, M. Selvakumar, Y. N. Sudhakar, and M. G. Mahesha, "Review on persistent challenges of perovskite solar cells' stability," *Solar Energy*, vol. 218, pp. 469–491, 2021, doi: 10.1016/j.solener.2021.03.005.

[7] M. V. Khenkin, K. M. Anoop, E. A. Katz, and I. Visoly-Fisher, "Bias-dependent degradation of various solar cells: Lessons for stability of perovskite photovoltaics," *Energy and Environmental Science*, vol. 12, no. 2, pp. 550–558, 2019, doi: 10.1039/c8ee03475c.

[8] H. Guthrey and J. Moseley, "A Review and Perspective on Cathodoluminescence Analysis of Halide Perovskites," *Advanced Energy Materials*, vol. 10, no. 26, 2020, doi: 10.1002/aenm.201903840.

[9] Samuel Berweger, Gang Qiu, Yixiu Wang, Benjamin Pollard, Kristen L. Genter, Robert Tyrrell-Ead, T. Mitch Wallis, Wenzhuo Wu, Peide D. Ye, Pavel Kabos, Imaging Carrier Inhomogeneities in Ambipolar Tellurene Field Effect Transistors, Nano Lett 19(2), 2019, 1289, 10.1021/acs.nanolett.8b04865

[10] M. Al-Jassim and N. Haegel, Eds., Advanced Characterization of Thin Film Solar Cells. Institution of Engineering and Technology, 2020. [Online]. Available: https://digital-library.theiet.org/content/books/po/pbpo166e

[11] T. Minemoto, Y. Kawano, T. Nishimura, and J. Chantana, Numerical reproduction of a hybrid perovskite solar cell by device simulation considering band gap grading, Opt. Mater., 92, 60–66, Jun. 2019, 10.1016/j.optmat.2019.03.048

[12] Amit H. Munshi, Jason Kephart, Ali Abbas, John Raguse, Jean-Nicolas Beaudry, Kurt Barth, James Sites, John Walls, Walajabad Sampath, Polycrystalline Cd(Se,Te)/CdTe Absorber Cells With 28 mA/cm 2 Short-Circuit Current, IEEE Journal of Photovoltaics., 8(1), 2018, 310–314, 10.1109/jphotov.2017.2775139

[13] M. Burgelman, K. Decock, S. Khelifi, and A. Abass, Advanced electrical simulation of thin film solar cells, Thin Solid Films, 535, 2013, 296, 10.1016/j.tsf.2012.10.032

[14] J. Yang and S.-H. Wei, First-principles study of the band gap tuning and doping control in CdSe x Te1-x alloy for high efficiency solar cell, Chin. Phys. B, 28(8), 2019, 086106, 10.1088/1674-1056/28/8/086106
[15] C.-S. Jiang, D. Albin, M. Nardone, K.J. Howard, A. Danielson, A. Munshi, T. Shimpi, C. Xiao, H.R. Moutinho, M.M. Al-Jassim, G. Teeter, W. Sampath, Electrical potential investigation of reversible metastability and irreversible degradation of CdTe solar cells, Solar Energy Materials & Solar Cells. 238, 2022, 111610, 10.1016/j.solmat.2022.111610, 1845682
[16] C.-S. Jiang, M. A. Contreras, I. Repins, H. R. Moutinho, Y. Yan, M. J. Romero, L. M. Mansfield, R. Noufi, M. M. Al-Jassim, How grain boundaries in Cu(In,Ga)Se2 thin films are charged: Revisit, Applied Physics Letters, 101, 2012, 033903, 10.1063/1.4737406
[17] C.-S. Jiang, L. M. Mansfield, S. Glynn, C. Xiao, R. Garris, S. Christensen, M. Al-Jassim, Effect of Window-Layer Materials on p-n Junction Location in Cu(In,Ga)Se2 Solar Cells, IEEE Journal of Photovoltaics, 9, 2019, 308, 10.1109/jphotov.2018.2874039, 1480235
[18] C.-S. Jiang, Z. G. Li, H. R. Moutinho, L. Liang, A. Ionkin, M. M. Al-Jassim, Real-space microscopic electrical imaging of n+-p junction beneath front-side Ag contact of multicrystalline Si solar cells, Journal of Applied Physics, 111, 2012, 083704, 10.1063/1.4703923
[19] Giles E. Eperon, Kevin H. Stone, Laura E. Mundt, Tracy H. Schloemer, Severin N. Habisreutinger, Sean P. Dunfield, Laura T. Schelhas, Joseph J. Berry, David T. Moore, The role of dimethylammonium in bandgap modulation for stable halide hybrid perovskites, ACS Energy Letters, 5(6), 2020, 1856, 10.1021/acsenergylett.0c00872
[20] C. M. Wolff, F. Zu, A. Paulke, L. P. Toro, N. Koch, and D. Neher, Reduced Interface-Mediated Recombination for High Open-Circuit Voltages in CH3NH3PbI3 Solar Cells, Advanced Materials, 29(28),2017, 1700159, 10.1002/adma.201700159
[21] D. Zhao, M. Sexton, H.-Y. Park, G. Baure, J. C. Nino, and F. So, High-efficiency solution-processed planar hybrid perovskite solar cells with a polymer hole transport layer, Advanced Energy Materials, 5(6), 2015, 1401855, 10.1002/aenm.201401855
[22] T. Golubev, D. Liu, R. Lunt, and P. Duxbury, Understanding the impact of C60 at the interface of hybrid perovskite solar cells via drift-diffusion modeling, AIP Advances, 9(3), 2019, 035026, 10.1063/1.5068690
[23] Axel F. Palmstrom, Giles E. Eperon, Tomas Leijtens, Rohit Prasanna, Severin N. Habisreutinger, William Nemeth, E. Ashley Gaulding, Sean P. Dunfield, Matthew Reese, Sanjini Nanayakkara, Taylor Moot, Jérémie Werner, Jun Liu, Bobby To, Steven T. Christensen, Michael D. McGehee, Maikel F.A.M. van Hest, Joseph M. Luther, Joseph J. Berry, David T. Moore, Enabling flexible all-perovskite tandem solar cells, Joule, 3(9), 2019, 2193, 10.1016/j.joule.2019.05.009
[24] Martin Stolterfoht, Christian M. Wolff, José A. Márquez, Shanshan Zhang, Charles J. Hages, Daniel Rothhardt, Steve Albrecht, Paul L. Burn, Paul Meredith, Thomas Unold, Dieter Neher, Visualization and suppression of interfacial recombination for high-efficiency large-area pin hybrid perovskite solar cells, Nature Energy, 3(10), 2018, 847, 10.1038/s41560-018-0219-8

[25] P. Zhao et al., “Numerical simulation of planar heterojunction hybrid perovskite solar cells based on SnO2 electron transport layer,” ACS Appl. Energy Mater., 2019, 10.1021/acsaem.9b00755.s001
[26] J. Tong, Q. Jiang, A. J. Ferguson, A. F. Palmstrom, F. Zhang, J. Hao, S. P. Dunfield, A. E. Louks, H. Lu, R. M. France, S. A. Johnson, M. Yang, J. F. Geisz, M. D. McGehee, M. C. Beard, D. Kuciauskas, J. J. Berry, and K. Zhu, Cation-engineered carrier control in efficient Sn-Pb narrow-bandgap hybrid perovskite tandem solar cells, Nature Energy, submitted, 1873671
[27] B.M. Wieliczka, J.A. Márquez, A.M. Bothwell, Q. Zhao, T. Moot, K.T. VanSant, A.J. Ferguson, T. Unold, D. Kuciauskas, and J.M. Luther, Probing the Origin of the Open Circuit Voltage in Hybrid perovskite Quantum Dot Photovoltaics, ACS Nano, 15(12), 2021, 19334, 10.1021/acsnano.1c05642, 1836035